
Conditional Variable Flow Matching: Transforming Conditional Densities with Amortized Conditional Optimal Transport

Adam P. Generale^{1,2}, Andreas E. Robertson³, Surya R. Kalidindi^{1,2}

¹Georgia Institute of Technology, ²Multiscale Technologies,

³Sandia National Laboratories

agenerale3@gatech.edu

aerober@sandia.gov

surya.kalidindi@me.gatech.edu

Abstract

Forecasting conditional stochastic nonlinear dynamical systems is a fundamental challenge repeatedly encountered across the biological and physical sciences. While flow-based models can impressively predict the temporal evolution of probability distributions representing possible outcomes of a specific process, existing frameworks cannot satisfactorily account for the impact of conditioning variables on these dynamics. Amongst several limitations, existing methods require training data with paired conditions and are developed for discrete conditioning variables. We propose *Conditional Variable Flow Matching* (CVFM), a framework for learning flows transforming conditional distributions with amortization across continuous conditioning variables – permitting predictions across the conditional density manifold. This is accomplished through several novel advances. In particular, simultaneous sample conditioned flows over the main and conditioning variables, alongside a conditional Wasserstein distance combined with a loss reweighting kernel facilitating conditional optimal transport. Collectively, these advances allow for learning system dynamics provided measurement data whose states and conditioning variables are not in correspondence. We demonstrate CVFM on a suite of increasingly challenging problems, including discrete and continuous conditional mapping benchmarks, image-to-image domain transfer, and modeling the temporal evolution of materials internal structure during manufacturing processes. We observe that CVFM results in improved performance and convergence characteristics over alternative conditional variants.

1 Introduction

Appropriately modeling the time-dependent evolution of distributions is a central goal in multiple scientific fields, such as single-cell genomics [1, 2], meteorology [3], robotics [4, 5], and materials science [6, 7]. In the sciences, forecasting stochastic nonlinear dynamical systems requires a methodology for learning the transformations of time-evolving densities given *unpaired* observational samples¹, or observations across time which are not in correspondence. This requirement arises due to practical constraints on data collection in such applications. For example, in both single-cell genomics and materials science, experimental testing to quantify the system’s

¹For unconditioned distributions, *unpaired* samples refers to the ability to sample from time marginal distributions independently, $x_0 \sim p_0(x)$ and $x_1 \sim p_1(x)$, rather than the joint, $p(x_0, x_1)$.

state is often destructive, precluding measurement of the state of a single sample across multiple time steps [1, 2, 8, 9].

Various approaches to address this challenge have recently been proposed, including diffusion Schrödinger bridges (DSB) [2, 10–13] alongside extensions of Flow Matching (FM) [1, 14]. These approaches generalize denoising diffusion probabilistic models [15], score matching [16], and FM [17–19], to arbitrary source distributions – a necessary relaxation to model the evolutionary pathways of physical or biological systems, as such natural systems rarely exhibit Gaussian source distributions².

Despite the apparent success of such approaches, their practical utility has been limited, as they solely permit the simulation of evolving unconditional distributions. However, in modeling the dynamics of real systems, the most critical questions often take the form of *how might an intervention affect the resulting dynamics?* For example, the dynamics of materials manufacturing processes depend upon process parameters such as applied temperature or power [20, 21]. Such questions require modeling the evolution of conditional distributions. Once more, we are restricted by our limited ability to observe their time-dependent states. In addition to unpaired state measurements, we often face the challenge of unpaired conditioning, which we define as the scenario in which data observed at discrete times frames possesses conditioning variables which are similarly unpaired. Formally, observed samples are drawn independently from their respective joint distributions at the initial and final time steps³ as $(x_0, y_0) \sim p_0(x, y), (x_1, y_1) \sim p_1(x, y)$ where there is no guarantee that $y_0 = y_1$, distinguishing this from traditional conditional settings where a fixed y is observed. Aside from the destructive nature of common data collection in the sciences, unpaired conditioning commonly arises due to the prohibitive costs of sample acquisition. Design-of-experiments or active learning approaches are frequently employed to mitigate these costs by minimizing the number of experiments – identifying a series of maximally informative test configurations [22, 23]. This diversity ensures that conditioning is purposefully rarely repeated.

Extensions modeling the dynamics of conditional distributions are still in their infancy [24–29]. Conditional input convex neural networks (ICNN) [26–28] and initial conditional extensions of flow matching [25, 29, 30], in particular, require datasets with matching conditioning, or the ability to first be able to select $y \in \mathcal{Y}$ and subsequently sample $x_t \sim p_t(x|y)$. This structure degrades in the limit of continuous conditioning variables, where obtaining multimarginal samples with equivalent conditioning is infeasible. Select recent works have begun to explore extensions enabling such continuous conditional treatment through conditional optimal transport (OT) between densities, although further development is necessary to scale them to high-dimensional problems [31, 32]. Similar approaches derived from measure theory have been also been integrated with FM to enable conditional transport [33, 34]. Although, our framework shares many high level proposals with these concurrent works [33], our increased development facilitating conditional OT proves to be immensely practically important. We motivate our framework and algorithm’s design by presenting a novel derivation which uncovers and highlights the critical role of such optimal couplings in the flow over the conditioning variable. In practice, we build around this observation; the multiple proposed elements designed to emphasize OT – the conditional Wasserstein distance and loss reweighting kernel – combine to significantly increase framework stability and performance.

We propose *Conditional Variable Flow Matching (CVFM)*, a general approach for learning the flow between source and target conditional distributions. Importantly, CVFM supports *entirely unpaired datasets*, wherein neither the sample data nor their corresponding conditioning variables need to be paired. We motivate the proposed CVFM algorithm through a theoretical analysis of the stability of flow matching on conditional densities, revealing the need for optimal transport over the conditioning variables. To realize this, core to CVFM is the usage of two conditional flows, a conditional Wasserstein distance, and a condition dependent loss reweighting kernel, generalizing existing simulation-free objectives for continuous normalizing flows (CNF) [17, 18] and stochastic dynamics [1, 35] to the conditional setting. We specifically focus on dynamics wherein the marginal distribution over the conditioning variable remains constant – a common setting in applied problems. The algorithm is introduced in the dynamical formulation of optimal

²We note that when approximating the dynamics of real systems, the model is trained to transform the state density between successive time steps. Therefore, even if the density at $t = 0$ is Gaussian, the bridge between arbitrary time steps must be generalized.

³These times can be fictitious (as in standard generative models, [14]) or can refer to the real time between time steps (as in dynamics, [1]).

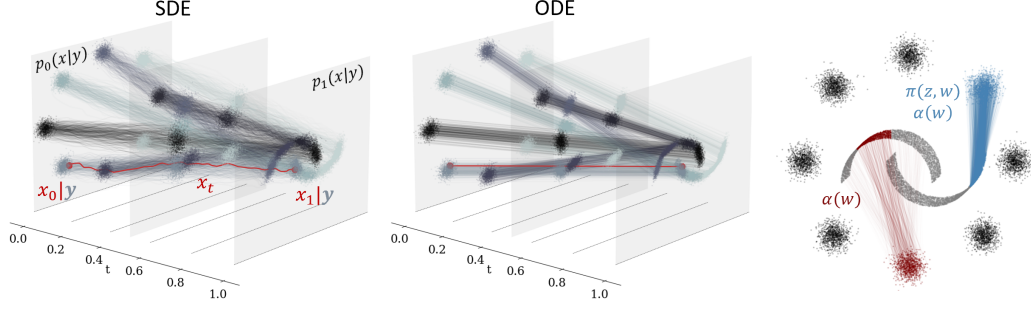


Figure 1. (Left) Conditional time-dependent density evolution from 8-Gaussians to Moons through the SDE and ODE formulations of CVFM. (Right) Comparison of conditional kernel in isolation (**red**) and the proposed CVFM framework (**blue**). The kernel effectively further facilitates disentanglement of the flow conditioning during static conditional OT.

transport (OT), augmenting FM and ordinary differential equation (ODE) based transport in defining a straightforward training objective for learning amortized conditional vector fields. Our objective facilitates simulation across the conditional density manifold, leveraging a conditional Wasserstein distance and kernel for enabling conditional OT. Subsequently, we analyze CVFM on several toy problems, demonstrating its superior performance and convergence behavior compared to existing methods. The performance of CVFM is further demonstrated in two more challenging case studies: the dynamics of material microstructure evolution conditioned on various manufacturing processes, and class conditional image-to-image mapping. As a part of these latter case studies, we further demonstrate the applicability of our method to approximating conditional Schrödinger bridges with a score-based stochastic differential equation (SDE) extension to FM [1].

2 Dynamic Mass Transport Methods

2.1 Flow Matching

Continuous Normalizing Flows (CNF) [36] define a mapping between distributions $x_0 \sim p_0(x)$ and $x_1 \sim p_1(x)$ both on the same domain, $x_0, x_1 \in \mathbb{R}^N$ via the following ordinary differential equation (ODE).

$$\frac{d}{dt}\phi_t(x) = u_t(\phi_t(x)), \quad \phi_0(x) = x \quad (1)$$

This ODE defines a flow, $\phi_t(x) = \phi(x, t)$, producing a push-forward operation for transforming an initial distribution, $p_0(x)$, into an arbitrary time dependent distribution, $p_t(x)$, (i.e., $\phi_\# : [0, 1] \times \mathcal{P}(\mathbb{R}^N) \rightarrow \mathcal{P}(\mathbb{R}^N)$), such that $p_t(x)$ is equal to $p_1(x)$ at $t = 1$ [17–19]. Individual samples $x_0 \sim p_0(x)$ can be transformed to $x_1 \sim p_1(x)$ by integrating the vector field $u_t : [0, 1] \times \mathbb{R}^N \rightarrow \mathbb{R}^N$ and solving the ODE in Eq. (1).

Flow matching (FM) provides a simulation-free objective for constructing the *marginal probability path* $p_t(x)$ via a marginalization of sample conditioned probability paths $p_t(x|z)$, conditioned on observations $z = (x_0, x_1)$ drawn from the empirical distributions – distributions defined implicitly by a set of observed data at the initial and final time steps, $q(x_0)$ and $q(x_1)$. Lipman et al. [17] demonstrates that one can similarly marginalize over conditional vector fields $u_t(x|z)$ to construct $u_t(x)$ which generates the probability flow $p_t(x)$ (Theorem 1 [17]). The consequences of which permit directly regressing upon the conditional vector field as

$$\mathcal{L}_{\text{CFM}}(\theta) = \mathbb{E}_{t, q(z), p_t(x|z)} \|v_\theta(x, t) - u_t(x|z)\|^2 \quad (2)$$

where for conditional Gaussian paths $p_t(x|z) = \mathcal{N}(x|\mu_t(z), \sigma_t^2(z))$ of $\phi_{t,z}(x) = \mu_t(z) + \sigma_t(z)x$ the unique conditional vector field $u_t(x|z)$ can be solved in closed form (Theorem 3 [17], Theorem 2.1, [18]).

2.2 Optimal Transport

The optimal transport (OT) problem aims to identify a mapping between measures, ν and μ , with minimal displacement cost [37]. The Kantorovich relaxation attempts to recover the OT coupling π given the potential set of all couplings on $\mathbb{R}^N \times \mathbb{R}^N$, such that the coupling's marginals are the original distributions, $\Pi(\mu, \nu) = \{\pi \in \mathcal{P}(\mathcal{X} \times \mathcal{Y}) : P_{\mathcal{X}\#}\pi = \mu \text{ and } P_{\mathcal{Y}\#}\pi = \nu\}$. The resulting distance $W(\mu, \nu)$ is the Wasserstein distance

$$W(\mu, \nu) = \inf_{\pi \in \Pi(\mu, \nu)} \int c(x, y) \pi(x, y) dx dy \quad (3)$$

where the squared Wasserstein-2 distance $W(\mu, \nu)_2^2$ is induced by the ground cost $c(x, y)^2$.

Entropically-Regularized OT: The optimization of the Wasserstein distance over couplings $\Pi(\mu, \nu)$ is a computationally challenging problem. The seminal work by Cuturi [38] alleviates these issues by introducing a regularization term using the Shannon entropy $H(\pi)$, equivalently described by the KL-divergence $\text{KL}(\pi \| \mu \otimes \nu)$ between a coupling, π and independent joint distribution between μ and ν , $\mu \otimes \nu$ [39].

$$W_\varepsilon(\mu, \nu) = \inf_{\pi \in \Pi(\mu, \nu)} \int c(x, y) \pi(x, y) dx dy - \varepsilon \text{KL}(\pi \| \mu \otimes \nu) \quad (4)$$

As $\varepsilon \rightarrow 0$ we recover the Kantorovich optimal transport plan, which we will distinguish as *exact optimal transport*, while $\varepsilon > 0$ yields a differentiable approximation to Eq. (3) with respect to the inputs.

OT-FM: While the Gaussian conditional probability paths for $p_t(x|z)$ in FM are the OT paths after conditioning on z [40], the induced marginal flow, defining $p_t(x)$, does not provide OT between distributions. Recent works have demonstrated that *dynamic* marginal OT can be achieved through identifying the *static* OT map [14, 41]. Practically, this is achieved by sampling z according to the OT coupling, π^* , between empirical marginal distributions, $q(z) = \pi^*(x_0, x_1)$. In practical implementations, π^* is identified within mini-batches during training. A core benefit of this approach is a pronounced reduction in variance of the regression target in Eq. (2), enabling expedited model convergence.

2.3 Schrödinger Bridge

The Schrödinger bridge problem aims to identify the most likely stochastic mapping between arbitrary marginal distributions $\mathbb{P}_0 = \mu_0$ and $\mathbb{P}_1 = \mu_1$ with respect to a given reference process \mathbb{Q} [38, 42, 43], defined as $\mathbb{P}_t^* = \text{argmin}_{\mathbb{P}_0 = \mu_0, \mathbb{P}_1 = \mu_1} \text{KL}(\mathbb{P}_t \| \mathbb{Q}_t)$. Frequently, \mathbb{Q} is taken to be $\mathbb{Q} = \sigma \mathbb{W}$, where \mathbb{W} is standard Brownian motion, otherwise known as the *diffusion Schrödinger bridge* [2, 12, 35, 44, 45].

Prior work has elucidated a rich relationship between the Schrödinger bridge problem and OT, in particular entropy-regularized OT [42, 46–48]. More specifically, with the reference process assumed as standard Brownian motion, the marginals of the dynamic Schrödinger bridge can be considered to be a mixture of Brownian bridges weighted by the *static* entropic OT map [42, 48]

$$p_t(x) = \int p_t(x|z) d\pi_\varepsilon^*(z). \quad (5)$$

In this reframing, the diffusion Schrödinger bridge can be approximated through a collection of marginal Brownian bridges defined as $p_t(x|z) = \mathcal{N}(x; (1-t)x_0 + tx_1, \sigma^2 t(1-t))$, with diffusion coefficient σ ; a construction reminiscent to the marginalization of probability paths in FM.

2.4 Score and Flow Matching

Given the notable connection between the Schrödinger bridge problem [43] and entropy regularized optimal transport [42, 46–48], a natural step to address this challenge in a simulation-free manner is to seek an extension to the OT-FM objective. Tong et al. [1] recently demonstrated the feasibility

of this approach through generalizing Eq. (2) to simultaneously regress on the conditional drift and score of an SDE. The proposed method replaces the flow ODE with the general Itô SDE $dx = u_t(x)dt + g(t)dw_t$ where $u_t(x)$ is the SDE drift, dw_t is standard Brownian motion⁴, and $g(t)$ is a handcrafted function frequently taken to be constant [1]. The SDE drift and a corresponding ODE vector field $\hat{u}_t(x)$ are intimately related by the expression

$$\hat{u}_t(x) = u_t(x) - \frac{g(t)^2}{2} \nabla \log p_t(x) \quad (6)$$

denoted as the *probability flow* ODE of the process [16], such that specification of the probability flow and score function are sufficient to describe the SDE [1].

Mirroring the previous flow-based models, the vector field, $u_t(x)$, and the score function, $s_t(x) = \nabla \log p_t(x)$, which define the SDE’s drift are unknown. Tong et al. [1] propose a generalization of the FM objective, Eq. (2), for training approximators of both objects

$$\mathcal{L}_{\text{SF}^2\text{M}}(\theta) = \mathcal{L}_{\text{CFM}}(\theta) + \mathbb{E}_{t,q(z),p(x|z)} \lambda(t)^2 \|s_\theta(x, t) - \nabla \log p_t(x|z)\|^2 \quad (7)$$

where $\lambda(t)^2$ is selected to standardize the loss, such that values of $\nabla \log p_t(x|z)$ near $t = 0$ or $t = 1$ do not dominate, effectively stabilizing training [1, 15, 16, 49]. Theorem 3.1 of their work demonstrates the feasibility of extending the marginalization construction of vector fields to the marginal score through matching of the conditional score of Brownian bridge probability paths. Further background can be found in Appendix B.

In modeling the dynamics of real world systems, such score and flow matching models have displayed improved performance over OT-FM and FM [1], in part due to the score function reducing movement to sparse regions of the data manifold. We emphasize that the conceptual similarity between the derivation of the flow matching objective and the generalized score and flow matching objective signifies that any improvements in the first can be readily transferred to the second without significant modification. As a result, in this work we theoretically restrict ourselves to purely flow-based models to simplify communication of novel developments, while in later case studies we utilize score and flow-based models.

3 Conditional Variable Flow Matching

In the following section, we generalize the FM objective in Eq. (2) to matching the flow between arbitrary conditional distributions, $p_0(x|y)$ to $p_1(x|y)$, provided *unpaired* observations with distinct conditioning variables.

3.1 Constructing Conditional Probability Paths and Vector Fields

We begin by first noting that the original marginalization motivating the flow matching objective can be extended to construct a probability flow across both x and a conditioning variable y as

$$p_t(x|y) = \int p_t(x|y, z, w) q(z, w) dz dw \quad (8)$$

where $q(z, w)$ now denotes the empirical distribution over $z = (x_0, x_1)$ and $w = (y_0, y_1)$, where samples are drawn from $x_0, y_0 \sim q(x_0, y_0)$ and $x_1, y_1 \sim q(x_1, y_1)$. We make the further assumption that the conditional joint probability path decomposes as $p_t(x, y|z, w) = p_t(x|z)p_t(y|w)$, resulting in two simultaneous conditional flows. In other words, we assume that the joint distribution at intermediate times, $p_t(x, y)$, retains a dependency between x and y defined by the joint discrete time empirical distributions.

We can also extend this line of thought towards defining a marginal conditional vector field, through marginalizing over vector fields conditioned on observations z and w as

⁴The Brownian motion differential is defined to be standard Gaussian noise times a time differential.

$$u_t(x|y) = \mathbb{E}_{q(z,w)} \frac{u_t(x|z)p_t(x|z)p_t(y|w)}{p_t(x,y)} \quad (9)$$

where $u_t(x|z) : \mathbb{R}^N \rightarrow \mathbb{R}^N$ is a conditional vector field generating $p_t(x|z)$ from $p_0(x|z)$, without any explicit dependence upon the conditional distribution over our conditional variable, y . Following Theorem 3 [17], Theorem 2.1, [18], and Theorem 3.1 [1], we prescribe a form to both conditional vector fields such that they generate their respective conditional probability distributions⁵. This method of combining conditional vector fields can be shown to generate the marginal conditional vector field, $u_t(x|y)$, which is formalized in the following theorem.

Theorem 3.1 *The marginal conditional vector field Eq. (9) generates the marginal conditional probability path Eq. (8) from $p_0(x|y)$ given samples of $q(z, w)$ if $q(y_0) = q(y_1)$ and (x_0, y_0) and (x_1, y_1) are drawn from $q(z, w)$ following the conditional optimal coupling $\pi(y_0, y_1)$ over w .*

Equality of the empirical distributions refers to equality in the underlying distribution, not the sample sets which define them implicitly. This result deviates from prior results in standard Flow Matching by Lipman et al. [17] (Theorem 1) and Albergo et al. [50] (Theorem 2.6) as well as recent concurrent studies in flow matching for conditional densities [34]; the theorem states that optimal transport over the conditioning variable is necessary for learning amortized conditional vector fields. Our framework is designed specifically to implement this conclusion. Through this lens, we will see the practical implications on learned mappings and training dynamics when this result is violated. The full proof of all theorems are provided in Appendix A.

3.2 Flow Matching for Conditional Distributions

Even provided Eq. (8) and Eq. (9), their incorporation in an overall objective for training a neural network approximator to $u_t(x|y)$ is still limited by several intractable integrals. Instead, we can obtain an unbiased estimator of the marginal conditional vector field and resulting probability path provided only samples from known distributions and the ability to compute $u_t(x|z)$ through the proposed conditional variable flow matching objective.

$$\mathcal{L}_{\text{CVFM}}(\theta) = \mathbb{E}_{t,q(z,w),p_t(x|z)p_t(y|w)} [\alpha(w) \|v_\theta(x, y, t) - u_t(x|z)\|^2] \quad (10)$$

The scaling term $\alpha(w)$ introduced dynamically modulates the acceptance of conditioning pairs, further facilitating conditional OT. This is formalized in the following recognizable theorem.

Theorem 3.2 *If $p_t(x|y) > 0$ for all $x \in \mathbb{R}^N$ and for all $y \in \mathbb{R}^M$ and $t \in [0, 1]$, then $\mathcal{L}_{\text{MCFM}}(\theta)$ (r.h.s. below) and $\mathcal{L}_{\text{CVFM}}(\theta)$ are equal up to a constant, and hence:*

$$\nabla_\theta \mathcal{L}_{\text{CVFM}}(\theta) = \nabla_\theta \mathbb{E}_{t,p_t(x,y)} \|v_\theta(x, y, t) - u_t(x|y)\|^2 \quad (11)$$

3.3 Stabilizing and Accelerating Training

Unlike previous flow matching frameworks, the empirical distribution, $q(z, w)$, cannot be sampled arbitrarily [1, 17]. Instead, samples must be drawn such that $w = (y_0, y_1)$ follows the optimal coupling $\pi(y_0, y_1)$. The theoretical reasons for this restriction are described in Appendix A. Although the construction of $q(z|w)$ is arbitrary, the conditional OT coupling $\pi(z|w)$ provides reduced objective variance and quicker convergence characteristics. We present two components of the CVFM framework specifically targeted towards enforcing OT in the conditioning space (Theorem 3.1).

Conditional Optimal Transport: We modify the empirical distribution, $q(z, w)$, through identifying a static conditional OT map: $q(z, w) = \pi(z, w)$ between the source and target

⁵For Gaussian probability paths with deterministic dynamics: $u_t(x|z) = x_1 - x_0$ [14, 18, 41] and stochastic dynamic: $\hat{u}_t(x|z) = ((1 - 2t)/(2t(1 - t)))(x - (tx_1 + (1 - t)x_0)) + (x_1 - x_0)$, $\nabla_x \log p_t(x|z) = (tx_1 + (1 - t)x_0 - x)/(\sigma^2 t(1 - t))$ [1].

distributions. Necessarily, the identification of this map requires the introduction of a ground cost with support over the space $\mathcal{X} \times \mathcal{Y} : \mathbb{R}^N \times \mathbb{R}^M$.

We would like to search for an OT map predominantly permitting movement across \mathcal{X} and not \mathcal{Y} . In a very practical sense, given the continuous support of \mathcal{Y} , such a constraint would not be feasible within a finite number of samples. Instead, we moderate this requirement in a manner similar to concurrent proposals by Kerrigan et al. [34], Chemseddine et al. [33], and Baptista et al. [32] in the form of the proposed continuous non-negative cost function

$$c((x_i, y_i), (x_j, y_j)) = \|x_i - x_j\|_p + \eta \|y_i - y_j\|_p \quad (12)$$

where $\eta > 0$ is a parameter governing the tolerance of transport permissible in \mathcal{Y} , and $\|x\|_p$ the p -norm.

Proposition 3.1 *Let $\mu, \nu \in \mathcal{P}(\mathbb{R}^N \times \mathbb{R}^M)$ and let π_η be an OT plan with associated value η from the cost function Eq. (12). As $\eta \rightarrow \infty$, mass transport in y is eliminated [51]:*

$$\lim_{\eta \rightarrow \infty} \int_{\mathbb{R}^M} \|y_i - y_j\|_p d\pi_\eta = 0 \quad (13)$$

In practice, the OT coupling is approximated in mini-batches. Samples $((x_0, y_0), (x_1, y_1)) \sim q(z, w)$ are drawn independently from the joint distributions at each boundary marginal, subsequently, couplings are sampled from the identified map which minimizes the proposed cost in Eq. (12).

Conditioning Mismatch: To further ensure that conditional OT is obtained within mini-batches, we include a dynamic scaling term through a stationary symmetric kernel $\alpha(w)$ in Eq. (10). The kernel scales the loss dependent upon the degree of mismatch in the sampled conditioning variable (y_0, y_1) – controlling the conditional probability flow permissible across y . In settings with discrete conditioning, we use a tight kernel approximating a delta function, prohibiting movement across classes, whereas with continuous conditioning greater relaxation is particularly advantageous. In this work, we restrict ourselves to the squared exponential kernel, $\alpha(w) = \exp(-\|y_0 - y_1\|_2^2 / 2\sigma_y^2)$ and the modulation of σ_y [52, 53]. See Appendix A for a theoretical analysis of the scaling kernel. We will repeatedly see that this addition is absolutely necessary and significantly improves model performance and training stability.

4 Experiments

We experimentally evaluate the performance of the proposed CVFM framework in accurately recovering target conditional densities on a suite of increasingly demanding problems. We first interrogate its performance on three 2D toy problems to baseline CVFM against alternate conditional methods, analyze its training stability, and visualize the learned flow paths. Subsequently, we demonstrate performance in higher dimensions by performing domain transfer between MNIST and FashionMNIST with discrete conditions. Lastly, we model the dynamics of materials’ microstructures undergoing spinodal decomposition across varied processing conditions. In this setting, we test the cumulative performance in mapping between a series of conditional distributions with continuous conditioning. For all case studies, we refer the interested reader to Appendix D for further motivation and problem construction and Appendix E for further analysis.

2D Experiments: We first evaluate the capabilities of various methods in approximating dynamic conditional optimal transport and the Schrödinger bridge (SB) problem in a low-dimensional setting. We consider three toy conditional problems: 8 Gaussians-Moons, 8 Gaussians-8 Gaussians, and Moons-Moons. The first involves 8 discrete conditions and flows with large bifurcations, Figure 2. The second also involves 8 discrete conditions, but contains flows with stronger dependence between x and y , Figure E.1. These two allow us to compare CVFM with previous methods. Finally, the third involves continuous conditioning. We compare our complete method, CVFM, against Conditional Generative Flow Matching (CGFM) [25, 29, 30], Triangular Conditional Optimal Transport (T-COT-FM) [34], as well as two ablated CVFM variants. CGFM in particular does not support *unpaired* conditioning, requiring the ability to sample from $z \sim \{\pi(x_0, x_1 | y_i)\}_{i=0}^m$, precluding

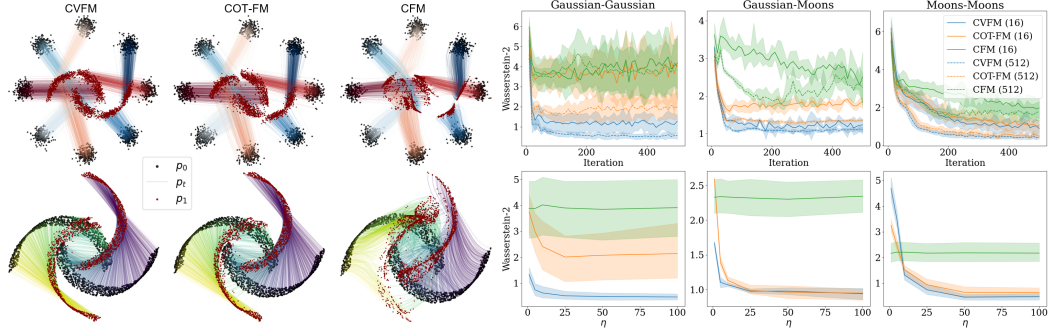


Figure 2. CVFM results in lower error in Wasserstein-2 distance to target distribution across batch sizes and conditional cost weighting η , compared to COT-FM (Eq. (12)) or the naïve conditional implementation CFM. Trajectories are colored by conditioning variable.

Table 1. Comparison of conditional neural optimal transport and Schrödinger bridge methods. Reported metrics consist of the Wasserstein-2 error between the target distribution and simulated distribution at $t = 1$, and the normalized path energy of the time-evolving distribution. Training was repeated over 5 seeds, with values reported as $\mu \pm \sigma$. Best observed values with *unpaired conditioning* are bolded with second best denoted by an asterisk within OT and SB methods. *Entropic* OT couplings, Eq. (4) identified via the Sinkhorn algorithm are differentiated from default *Exact* couplings, Eq. (3).

	Wasserstein-2 Error (\downarrow)			Normalized Path Energy (\downarrow)		
	8 Gaussian-8 Gaussian	8 Gaussian-Moons	Moons-Moons	8 Gaussian-8 Gaussian	8 Gaussian-Moons	Moons-Moons
CVFM	0.571\pm0.139	0.440\pm0.097	1.102\pm0.047	0.109 \pm 0.039*	0.043\pm0.049	0.125\pm0.003
COT-FM	1.997 \pm 0.528*	0.537 \pm 0.115*	1.353 \pm 0.022	0.177 \pm 0.081	0.075 \pm 0.031*	0.135 \pm 0.004*
CFM	4.013 \pm 1.026	1.768 \pm 0.448	2.227 \pm 0.264	0.403 \pm 1.688	0.148 \pm 0.287	0.410 \pm 0.061
T-COT-FM	2.296 \pm 0.060	0.564 \pm 0.031	1.318 \pm 0.041*	0.063\pm0.024	0.081 \pm 0.006	0.209 \pm 0.023
CVFM-Entropic	0.409\pm0.080	0.414\pm0.109	1.018\pm0.031	0.064\pm0.040	0.022\pm0.037	0.088\pm0.013
COT-FM-Entropic	2.566 \pm 0.624	0.720 \pm 0.176	1.080 \pm 0.016*	0.179 \pm 0.073	0.073 \pm 0.064	0.125 \pm 0.004
CVSFM	0.518 \pm 0.105*	0.428 \pm 0.114*	1.081 \pm 0.028	0.089 \pm 0.033*	0.041 \pm 0.056*	0.115 \pm 0.013
COT-SFM	1.936 \pm 0.423	0.539 \pm 0.133	1.267 \pm 0.043	0.159 \pm 0.085	0.064 \pm 0.049	0.110 \pm 0.013*
CGFM	0.491 \pm 0.095	0.352 \pm 0.085	–	0.024 \pm 0.038	0.019 \pm 0.054	–
CGFM-Entropic	0.483 \pm 0.075	0.376 \pm 0.083	–	0.037 \pm 0.066	0.019 \pm 0.065	–

its ability to address scientific questions as $m \rightarrow \infty$. We simply present it as a useful benchmark, representing a lower-bound on the discrete conditioning problems presented. The first of the ablated variants considered removes both mini-batch conditional optimal transport and $\alpha(w)$, but retains the interpolated flow $p_t(y|w)$ (see Appendix D). We refer to this variant as Conditional Flow Matching (CFM) as it reduces to the original proposed CFM algorithm given paired samples [17, 18]. The second variant solely excludes $\alpha(w)$ – we refer to this as Conditional Optimal Transport Flow Matching (COT-FM). COT-FM is nearly equivalent to the concurrent work of Chemseddine et al. [33]; it differs by having varied noise schedules for the conditional probability paths $p_t(x|z)$ and $p_t(y|w)$. ODE and SDE-based variants for the SB problem are also evaluated for CVFM and COT-FM, utilizing the probability flow ODE with entropic regularized OT, alongside the SDE extension to our objective, conditional variable score and flow matching (CVSFM).

Three mappings are investigated and their associated results are displayed in Table 1, with the Wasserstein-2 error from the predicted distribution at $t = 1$ to the target distribution reported. The CVFM method notably results in equivalent or more optimal values of Wasserstein-2 error across all mappings with unpaired conditioning. CVFM even nearly matches CGFM’s performance on discrete problems, where CGFM has knowledge of the correct conditional couplings *a priori*. Figure 2 contrasts samples and pathways from a subset of these methods. Only CVFM is able to clearly recreate the final target distributions. Notably, the kernel appreciably improves performance; CVFM outperforms both T-COT-FM and COT-FM, while the CFM formulation highlights the importance of the sampling from the optimal coupling: its absence precludes the validity of Eq. (9) (Appendix A) resulting in poor performance.

Improved convergence: Beyond improved metrics, the CVFM implementation also displays improved convergence characteristics, as evidenced by Figure 2. In all cases, the CVFM objective

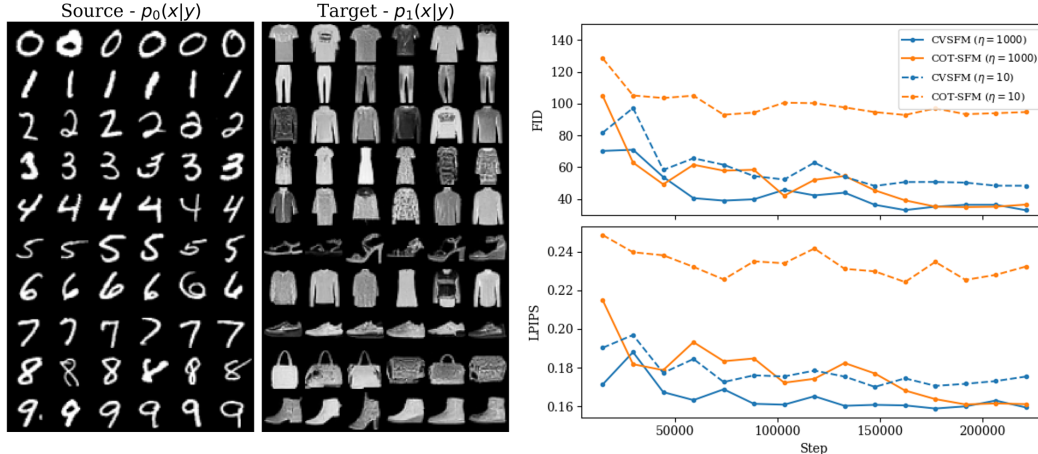


Figure 3. CVSFM conditionally generated images from the FashionMNIST dataset. (Left) pane displays samples from the initial distributions $p_0(x|y)$, while the middle displays generated samples from $p_1(x|y)$. Relative positioning indicates paired samples. (Right) pane illustrates the improved convergence of CVSFM over COT-SFM in high-dimensional domain transfer for $\eta = 10$ and $\eta = 1000$. Displayed FID/LPIPS scores are computed per class and averaged.

converges faster and to a lower metric value than other methods and variants. Further interrogation regarding the impact of η in the conditional ground cost and $\alpha(w)$ was also performed. In the proposed methods incorporating the ground cost (CVFM, COT-FM, and T-COT-FM), increasing η leads to improvement. However, it is often insufficient. For example, in the *8 Gaussian - 8 Gaussian* example the addition of $\alpha(w)$ in CVFM facilitates a marked improvement. Additional ablations are also presented in Appendix E.1 highlighting the important role of $\alpha(w)$ in reducing the error in the mini-batch COT approximation inherent in Eq. (12) in greater depth.

MNIST-FashionMNIST Domain Transfer: We further evaluate our method in high-dimensional domain transfer between MNIST digits and FashionMNIST clothing articles with conditioning by discrete class. We directly compare our two variants, CVSFM against COT-SFM, Figure 3. The FID and LPIPS scores reported are averages across the class conditioned scores (i.e., FID and LPIPS are computed on a per-class basis across 1,000 samples in each class). Select images from the source and corresponding generated images from the target conditional distributions are also shown. As seen in the repeated samples, the model is able to consistently map to the correct paired conditional distribution while displaying appreciable diversity within each class. Mirroring the 2D experiments, we observe improved convergence and mode coverage with CVSFM compared to COT-SFM across all η values due to $\alpha(w)$ restricting flow across y . For further analysis, see Appendix E.2.

Material Dynamics: We next investigate the performance of our proposed method in our target scientific application: the dynamics of time-evolving microstructures subject to various processing conditions. Phase-field simulations are commonly applied to model a number of manufacturing processes involving evolving interfaces (such as solidification/melting, spinodal decomposition, grain growth, recrystallization, and crack propagation [54, 55]). These simulations are stochastic – the result of numerical noise representing thermal fluctuations, such that, even provided equivalent initial processing conditions, the resulting microstructure state over time will vary. In this experiment, we particularly focus on spinodal decomposition, applicable for material systems which undergo a thermodynamic phase transition resulting in the separation of a homogeneous mixture into distinct phases. The resulting dataset contains 10,000 two-phase microstructures of dimension 256×256 voxels evaluated across 100 time steps. Quantification of the internal state of the material’s microstructures was performed by computing their 2-point spatial correlations [56, 57], a representation which quantifies internal spatial correlations between constituents in the material, while also accounting for underlying symmetries (e.g., translation-equivariance and periodicity). Further discussion regarding this quantification procedure is presented in Appendix C. These correlations were then finally compressed to a 5-dimensional vector via Principal Component Analysis (PCA). In this problem, we use CVFM to model conditional time-dependent microstructural evolution, provided 100 sequential conditional empirical distributions.

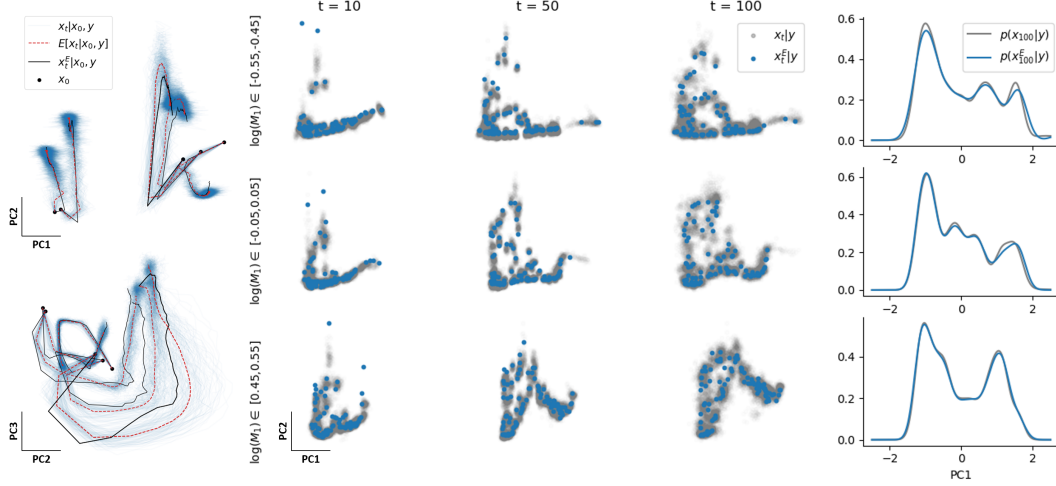


Figure 4. Collection of 5 randomly sampled trajectories from the test set in projections of PC1-PC2 and PC2-PC3 displaying (left) samples in blue from CVSFM-Exact, with the expected value as a function of time in red. Comparison of test marginal densities (middle) constructed as narrow subsets of first constituent’s mobility (\mathcal{M}_1) parameter, in PC1-PC2 projection, and (right) marginal comparison of final state at $t = 100$ for PC1. 128 samples were simulated for each (x_0, y) .

Importantly, the time-dependent observations modeled are the result of computational simulations rather than high-cost intermittent experimental sampling, granting us complete access to *paired* conditioning-trajectory information – information frequently unavailable in manufacturing settings of interest. This enables us to validate and quantify the model’s performance by computing error metrics on a per trajectory basis. Despite this, we still implement CVFM using *unpaired* data to mirror the experimental setting. Table 2 contrasts the absolute error, computed against the ground truth trajectories, of various potential surrogates for the dynamics. We compare CVFM – using *unpaired* samples and conditioning variables – against traditional approaches (Neural ODEs and LSTM) requiring complete trajectory information. Despite only having access to corrupted and *misaligned* versions of the available observations, CVSFM-Exact results in better performance, displaying lower mean absolute errors across expected trajectories. CVSFM-Exact also outperforms alternatives such as T-COT-FM [34] and two SDE-based extensions, denoted T-COT-SFM, improved using insights from this paper. The first SDE extension utilizes a fixed value of σ , while in the second, we extend the work of Kerrigan et al. [34] to set a distinct conditional probability path across y , with its own σ_y as implemented in this work.

We next examine CVFM’s ability to accurately learn the stochasticity in the process dynamics of the microstructure in a distributional sense. Because the conditioning variables are continuous, we only have one unique trajectory $\{(x_i, y_i)\}_{i=0}^{T=99}$ for each given y . To overcome this limitation, we defined three narrow subsets based on the first mobility parameter \mathcal{M}_1 , covering the test dataset. The remaining parameters (\mathcal{M}_2, c_0) are not constrained. Table 3 presents the time-averaged Wasserstein-2 errors across all observed marginals for variants of CVSFM and COT-SFM on these subsets. CVSFM accurately reconstructs the marginal distributions. Figure 4 displays sample trajectories, along with the evolving time distributions for these subsets, and their corresponding marginalized density estimates along the first principal component for CVSFM. The network captures the change in the width and shape of the distribution over time. Overall, the performance on individual trajectories and observed marginals highlights the proposed method’s effectiveness in capturing complex conditional stochastic nonlinear dynamics.

5 Conclusions

We have proposed a novel framework, capable of learning to transform conditional distributions between general source and target distributions given *unpaired* samples. With the same underlying approach, we have also presented extensions capable of approximating the conditional Schrödinger bridge problem. Our central contribution is a novel algorithmic framework for measures in

Table 2. Comparison of conditional neural optimal transport methods alongside conventional approaches on spinodal decomposition PC trajectories. Reported mean absolute errors are computed between predicted trajectories and target trajectories not observed during training across all times. Expected values, $\mathbb{E}[x_t|x_0, y]$, are used for stochastic predictions. Reported absolute error metrics are reported as $\mu \pm \sigma$ alongside maximum and minimum values.

	Train			Test		
	$\mu \pm \sigma$	Min.	Max.	$\mu \pm \sigma$	Min.	Max.
Neural ODE	0.261 \pm 0.119	0.105	1.499	0.264 \pm 0.129	0.116	1.400
LSTM	0.355 \pm 0.212	0.038	2.071	0.358 \pm 0.331	0.045	1.648
CVSFM	0.166\pm0.140	0.023	1.654	0.188\pm0.147	0.039	1.284
CVSFM-Entropic	0.378 \pm 0.322	0.045	2.112	0.388 \pm 0.320	0.044	2.032
COT-SFM	0.202 \pm 0.348	0.034	11.422	0.218 \pm 0.489	0.033	11.649
COT-SFM-Entropic	0.524 \pm 0.306	0.108	2.568	0.531 \pm 0.307	0.110	2.012
T-COT-FM	0.899 \pm 0.370	0.163	3.47	0.901 \pm 0.365	0.161	2.639
T-COT-SFM	0.636 \pm 0.279	0.235	2.331	0.637 \pm 0.282	0.194	2.335
T-COT-SFM (σ_y)	0.332 \pm 0.223	0.073	2.525	0.329 \pm 0.222	0.075	1.786

Table 3. Comparison of time-averaged Wasserstein-2 error between predicted marginal distributions and test data for binned mobility \mathcal{M}_1 values.

	Wasserstein-2 Error (\downarrow)		
	$\log(\mathcal{M}_1) \in [-0.55, -0.45]$	$\log(\mathcal{M}_1) \in [-0.05, 0.05]$	$\log(\mathcal{M}_1) \in [0.45, 0.55]$
CVSFM	0.637	0.628	0.646
CVSFM-Entropic	0.886	1.213	1.523
COT-SFM	0.674	0.608	0.690
COT-SFM-Entropic	1.129	1.329	1.997

a conditional Wasserstein space, equipped with a regularized conditional distance metric, an independent conditioning variable flow, and a scaling kernel enforcing structure across the learned vector fields in the conditioning variable. We verify our proposed approach through synthetic and real-world tasks, demonstrating stable training, high dimensional scaling, and, finally, demonstrating that CVFM is an effective, simulation-free framework for learning conditional stochastic dynamical processes from unpaired measurements.

Acknowledgments

The authors acknowledges funding by various sources. Adam P. Generale: Multiscale Technologies & Pratt & Whitney. Surya R. Kalidindi acknowledges funding from ONR N00014-18-1-2879 as well as all previously listed funding sources. This work utilized computing resources and services provided by the Partnership for an Advanced Computing Environment (PACE) at the Georgia Institute of Technology, Atlanta, Georgia, USA. Andreas E. Robertson acknowledges the Jack Kent Cooke Foundation. In addition, this article has been authored by an employee of National Technology & Engineering Solutions of Sandia, LLC under Contract No. DE-NA0003525 with the U.S. Department of Energy (DOE). The employee owns all right, title, and interest in and to the article and is solely responsible for its contents. The United States Government retains and the publisher, by accepting the article for publication, acknowledges that the United States Government retains a non-exclusive, paid-up, irrevocable, world-wide license to publish or reproduce the published form of this article or allow others to do so, for United States Government purposes. The DOE will provide public access to these results of federally sponsored research in accordance with the DOE Public Access Plan www.energy.gov/downloads/doe-public-access-plan.

Reproducibility

We have included several appendices describing in detail the theoretical derivations referenced in the paper (Appendix A) as well as describing the proposed algorithm (Appendix D) and the experiments (Appendix C, B, E, and D). Code utilized in this paper is provided at <https://github.com/agenerale/conditional-variable-flow-matching>.

References

- [1] Alexander Tong, Nikolay Malkin, Kilian Fatras, Lazar Atanackovic, Yanlei Zhang, Guillaume Huguët, Guy Wolf, and Yoshua Bengio. Simulation-free Schrödinger bridges via score and flow matching, October 2023. URL <http://arxiv.org/abs/2307.03672>. arXiv:2307.03672 [cs].
- [2] Charlotte Bunne, Ya-Ping Hsieh, Marco Cuturi, and Andreas Krause. The Schrödinger Bridge between Gaussian Measures has a Closed Form, March 2023. URL <http://arxiv.org/abs/2202.05722>. arXiv:2202.05722 [cs, q-bio].
- [3] Mike Fisher, Jorge Nocedal, Yannick Trémolet, and Stephen J. Wright. Data assimilation in weather forecasting: a case study in PDE-constrained optimization. *Optimization and Engineering*, 10(3):409–426, September 2009. ISSN 1389-4420, 1573-2924. doi: 10.1007/s11081-008-9051-5. URL <http://link.springer.com/10.1007/s11081-008-9051-5>.
- [4] Domènec Ruiz-Balet and Enrique Zuazua. Neural ODE Control for Classification, Approximation, and Transport. *SIAM Review*, 65(3):735–773, August 2023. ISSN 0036-1445. doi: 10.1137/21M1411433. URL <https://epubs.siam.org/doi/abs/10.1137/21M1411433>. Publisher: Society for Industrial and Applied Mathematics.
- [5] Yongxin Chen, Tryphon T. Georgiou, and Michele Pavon. Optimal Transport in Systems and Control. *Annual Review of Control, Robotics, and Autonomous Systems*, 4(Volume 4, 2021):89–113, May 2021. ISSN 2573-5144. doi: 10.1146/annurev-control-070220-100858. URL <https://www.annualreviews.org/content/journals/10.1146/annurev-control-070220-100858>. Publisher: Annual Reviews.
- [6] Surya R. Kalidindi. *Hierarchical Materials Informatics: Novel Analytics for Materials Data*. Butterworth-Heinemann, Amsterdam, 1st edition edition, August 2015. ISBN 978-0-12-410394-8.
- [7] Brent L. Adams, Surya R. Kalidindi, and David T. Fullwood. Microstructure-Sensitive Design for Performance Optimization. In *Microstructure Sensitive Design for Performance Optimization*, page i. Elsevier, 2013. ISBN 978-0-12-396989-7. doi: 10.1016/B978-0-12-396989-7.01001-7. URL <https://linkinghub.elsevier.com/retrieve/pii/B9780123969897010017>.
- [8] Reza Ghanavati and Homam Naffakh-Moosavy. Additive manufacturing of functionally graded metallic materials: A review of experimental and numerical studies. *Journal of Materials Research and Technology*, 13:1628–1664, July 2021. ISSN 2238-7854. doi: 10.1016/j.jmrt.2021.05.022. URL <https://www.sciencedirect.com/science/article/pii/S2238785421004622>.
- [9] ASTM International. Standard Test Methods and Definitions for Mechanical Testing of Steel Products, March 2024. URL <https://compass.astm.org/document/?contentCode=ASTM%7CA0370-24%7Cen-US&proxycl=https%3A%2F%2Fsecure.astm.org&fromLogin=true>.
- [10] Guan-Horng Liu, Tianrong Chen, Oswin So, and Evangelos Theodorou. Deep Generalized Schrödinger Bridge. *Advances in Neural Information Processing Systems*, 35:9374–9388, December 2022. URL https://proceedings.neurips.cc/paper_files/paper/2022/hash/3d17b7f7d52c83ab6e97e2dc0bda2e71-Abstract-Conference.html.
- [11] Tianrong Chen, Guan-Horng Liu, and Evangelos A. Theodorou. Likelihood Training of Schrödinger Bridge using Forward-Backward SDEs Theory, April 2023. URL <http://arxiv.org/abs/2110.11291>. arXiv:2110.11291 [cs, math, stat].
- [12] Valentin De Bortoli, James Thornton, Jeremy Heng, and Arnaud Doucet. Diffusion Schrödinger Bridge with Applications to Score-Based Generative Modeling. In *Advances in Neural Information Processing Systems*, volume 34, pages 17695–17709. Curran Associates, Inc., 2021. URL https://proceedings.neurips.cc/paper_files/paper/2021/hash/940392f5f32a7ade1cc201767cf83e31-Abstract.html.

- [13] Zhicong Tang, Tiankai Hang, Shuyang Gu, Dong Chen, and Baining Guo. Simplified Diffusion Schrödinger Bridge, March 2024. URL <http://arxiv.org/abs/2403.14623>. arXiv:2403.14623 [cs].
- [14] Alexander Tong, Nikolay Malkin, Guillaume Huguët, Yanlei Zhang, Jarrod Rector-Brooks, Kilian Fatras, Guy Wolf, and Yoshua Bengio. Improving and Generalizing Flow-Based Generative Models with Minibatch Optimal Transport. July 2023. URL <https://openreview.net/forum?id=HgDwiZrpVq>.
- [15] Jonathan Ho, Ajay Jain, and Pieter Abbeel. Denoising Diffusion Probabilistic Models, December 2020. URL <http://arxiv.org/abs/2006.11239>. arXiv:2006.11239 [cs, stat].
- [16] Yang Song, Jascha Sohl-Dickstein, Diederik P Kingma, Abhishek Kumar, Stefano Ermon, and Ben Poole. Score-based Generative Modeling Through Stochastic Differential Equations. 2021.
- [17] Yaron Lipman, Ricky T Q Chen, Heli Ben-Hamu, Maximilian Nickel, and Matt Le. Flow Matching for Generative Modeling. 2023.
- [18] Michael S. Albergo and Eric Vanden-Eijnden. Building Normalizing Flows with Stochastic Interpolants, March 2023. URL <http://arxiv.org/abs/2209.15571>. arXiv:2209.15571 [cs, stat].
- [19] Xingchao Liu, Chengyue Gong, and Qiang Liu. Flow Straight and Fast: Learning to Generate and Transfer Data with Rectified Flow, September 2022. URL <http://arxiv.org/abs/2209.03003>. arXiv:2209.03003 [cs].
- [20] Zhiyuan Liu, Dandan Zhao, Pei Wang, Ming Yan, Can Yang, Zhangwei Chen, Jian Lu, and Zhaoping Lu. Additive manufacturing of metals: Microstructure evolution and multistage control. *Journal of Materials Science & Technology*, 100:224–236, February 2022. ISSN 1005-0302. doi: 10.1016/j.jmst.2021.06.011. URL <https://www.sciencedirect.com/science/article/pii/S1005030221006046>.
- [21] George F. Schrader and Ahmad K. Elshennawy. *Manufacturing Processes and Materials, Fourth Edition*. Society of Manufacturing Engineers, 2000. ISBN 978-0-87263-517-3. Google-Books-ID: Nz2wXvmkAF0C.
- [22] Turab Lookman, Prasanna V. Balachandran, Dezhen Xue, and Ruihao Yuan. Active learning in materials science with emphasis on adaptive sampling using uncertainties for targeted design. *npj Computational Materials*, 5(1):1–17, February 2019. ISSN 2057-3960. doi: 10.1038/s41524-019-0153-8. URL <https://www.nature.com/articles/s41524-019-0153-8>. Publisher: Nature Publishing Group.
- [23] Anh Tran, John A. Mitchell, Laura P. Swiler, and Tim Wildey. An active learning high-throughput microstructure calibration framework for solving inverse structure–process problems in materials informatics. *Acta Materialia*, 194:80–92, August 2020. ISSN 1359-6454. doi: 10.1016/j.actamat.2020.04.054. URL <https://www.sciencedirect.com/science/article/pii/S1359645420303220>.
- [24] Jonathan Ho and Tim Salimans. Classifier-Free Diffusion Guidance, July 2022. URL <http://arxiv.org/abs/2207.12598>. arXiv:2207.12598 [cs].
- [25] Qinqing Zheng, Matt Le, Neta Shaul, Yaron Lipman, Aditya Grover, and Ricky T. Q. Chen. Guided Flows for Generative Modeling and Decision Making, December 2023. URL <http://arxiv.org/abs/2311.13443>. arXiv:2311.13443 [cs, stat].
- [26] Charlotte Bunne, Andreas Krause, and Marco Cuturi. Supervised Training of Conditional Monge Maps. *Advances in Neural Information Processing Systems*, 35:6859–6872, December 2022. URL https://proceedings.neurips.cc/paper_files/paper/2022/hash/2d880acd7b31e25d45097455c8e8257f-Abstract-Conference.html.
- [27] Benedek Harsanyi, Marianna Rapsomaniki, and Jannis Born. Learning Drug Perturbations via Conditional Map Estimators. March 2024. URL <https://openreview.net/forum?id=FE7lRuwmfI>.
- [28] Charlotte Bunne, Stefan G. Stark, Gabriele Gut, Jacobo Sarabia del Castillo, Mitch Levesque, Kjong-Van Lehmann, Lucas Pelkmans, Andreas Krause, and Gunnar Rätsch. Learning single-cell perturbation responses using neural optimal transport. *Nature Methods*, 20

- (11):1759–1768, November 2023. ISSN 1548-7105. doi: 10.1038/s41592-023-01969-x. URL <https://www.nature.com/articles/s41592-023-01969-x>. Publisher: Nature Publishing Group.
- [29] Noboru Isobe, Masanori Koyama, Kohei Hayashi, and Kenji Fukumizu. Extended Flow Matching: a Method of Conditional Generation with Generalized Continuity Equation, March 2024. URL <http://arxiv.org/abs/2402.18839>. arXiv:2402.18839 [cs, math].
 - [30] Quan Dao, Hao Phung, Binh Nguyen, and Anh Tran. Flow Matching in Latent Space, July 2023. URL <http://arxiv.org/abs/2307.08698>. arXiv:2307.08698 [cs].
 - [31] Esteban G. Tabak, Giulio Trigila, and Wenjun Zhao. Data Driven Conditional Optimal Transport, October 2019. URL <http://arxiv.org/abs/1910.11422>. arXiv:1910.11422 [math].
 - [32] Ricardo Baptista, Aram-Alexandre Pooladian, Michael Brennan, Youssef Marzouk, and Jonathan Niles-Weed. Conditional simulation via entropic optimal transport: Toward non-parametric estimation of conditional Brenier maps, November 2024. URL <http://arxiv.org/abs/2411.07154>. arXiv:2411.07154 [stat].
 - [33] Jannis Chemseddine, Paul Hagemann, Gabriele Steidl, and Christian Wald. Conditional Wasserstein Distances with Applications in Bayesian OT Flow Matching, June 2024. URL <http://arxiv.org/abs/2403.18705>. arXiv:2403.18705 [cs, math].
 - [34] Gavin Kerrigan, Giosue Migliorini, and Padhraic Smyth. Dynamic Conditional Optimal Transport through Simulation-Free Flows, May 2024. URL <http://arxiv.org/abs/2404.04240>. arXiv:2404.04240.
 - [35] Yuyang Shi, Valentin De Bortoli, Andrew Campbell, and Arnaud Doucet. Diffusion Schrödinger Bridge Matching, December 2023. URL <http://arxiv.org/abs/2303.16852>. arXiv:2303.16852 [cs, stat].
 - [36] Ricky T. Q. Chen, Yulia Rubanova, Jesse Bettencourt, and David K Duvenaud. Neural Ordinary Differential Equations. In *Advances in Neural Information Processing Systems*, volume 31. Curran Associates, Inc., 2018. URL https://proceedings.neurips.cc/paper_files/paper/2018/hash/69386f6bb1dfed68692a24c8686939b9-Abstract.html.
 - [37] Cédric Villani. *Optimal Transport*, volume 338 of *Grundlehren der mathematischen Wissenschaften*. Springer, Berlin, Heidelberg, 2009. ISBN 978-3-540-71049-3. doi: 10.1007/978-3-540-71050-9. URL <http://link.springer.com/10.1007/978-3-540-71050-9>.
 - [38] Marco Cuturi. Sinkhorn Distances: Lightspeed Computation of Optimal Transport. In *Advances in Neural Information Processing Systems*, volume 26. Curran Associates, Inc., 2013. URL https://papers.nips.cc/paper_files/paper/2013/hash/af21d0c97db2e27e13572cbf59eb343d-Abstract.html.
 - [39] Gabriel Khan and Jun Zhang. When Optimal Transport Meets Information Geometry. *Information Geometry*, 5(1):47–78, July 2022. ISSN 2511-2481, 2511-249X. doi: 10.1007/s41884-022-00066-w. URL <http://arxiv.org/abs/2206.14791>. arXiv:2206.14791 [cs, math].
 - [40] Gabriel Peyré and Marco Cuturi. Computational Optimal Transport, March 2020. URL <http://arxiv.org/abs/1803.00567>. arXiv:1803.00567 [stat].
 - [41] Aram-Alexandre Pooladian, Heli Ben-Hamu, Carles Domingo-Enrich, Brandon Amos, Yaron Lipman, and Ricky T. Q. Chen. Multisample Flow Matching: Straightening Flows with Minibatch Couplings, May 2023. URL <http://arxiv.org/abs/2304.14772>. arXiv:2304.14772 [cs].
 - [42] Christian Léonard. A survey of the Schrödinger problem and some of its connections with optimal transport, August 2013. URL <http://arxiv.org/abs/1308.0215>. arXiv:1308.0215 [math].
 - [43] E. Schrödinger. Sur la théorie relativiste de l’électron et l’interprétation de la mécanique quantique. *Annales de l’institut Henri Poincaré*, 2(4):269–310, 1932. ISSN 2400-4855. URL http://www.numdam.org/item/AIHP_1932__2_4_269_0/.

- [44] Yihui Chen, Yanfei Chen, Dawei Wang, and Shigang Ai. Generating 3D digital material twins for woven ceramic-matrix composites from uCT images. *Journal of the American Ceramic Society*, 105(1):481–497, 2022. ISSN 1551-2916. doi: 10.1111/jace.18044. URL <https://onlinelibrary.wiley.com/doi/abs/10.1111/jace.18044>. _eprint: <https://onlinelibrary.wiley.com/doi/pdf/10.1111/jace.18044>.
- [45] Francisco Vargas. Machine-learning approaches for the empirical Schrödinger bridge problem. Technical Report 958, University of Cambridge, June 2021.
- [46] Toshio Mikami and Michèle Thieullen. Duality theorem for the stochastic optimal control problem. *Stochastic Processes and their Applications*, 116(12):1815–1835, December 2006. ISSN 0304-4149. doi: 10.1016/j.spa.2006.04.014. URL <https://www.sciencedirect.com/science/article/pii/S0304414906000627>.
- [47] Toshio Mikami. Monge’s problem with a quadratic cost by the zero-noise limit of h-path processes. *Probability Theory and Related Fields*, 129(2):245–260, June 2004. ISSN 1432-2064. doi: 10.1007/s00440-004-0340-4. URL <https://doi.org/10.1007/s00440-004-0340-4>.
- [48] Christian Léonard. From the Schrödinger problem to the Monge-Kantorovich problem, November 2010. URL <https://arxiv.org/abs/1011.2564v1>.
- [49] Tero Karras, Miika Aittala, Timo Aila, and Samuli Laine. Elucidating the Design Space of Diffusion-Based Generative Models, October 2022. URL <http://arxiv.org/abs/2206.00364>. arXiv:2206.00364 [cs, stat].
- [50] Michael S. Albergo, Nicholas M. Boffi, and Eric Vanden-Eijnden. Stochastic Interpolants: A Unifying Framework for Flows and Diffusions, March 2023. URL <http://arxiv.org/abs/2303.08797>. arXiv:2303.08797 [cond-mat].
- [51] Guillaume Carlier, Alfred Galichon, and Filippo Santambrogio. From Knothe’s transport to Brenier’s map and a continuation method for optimal transport, October 2008. URL <http://arxiv.org/abs/0810.4153>. arXiv:0810.4153.
- [52] Andrew Gordon Wilson and Ryan Prescott Adams. Gaussian Process Kernels for Pattern Discovery and Extrapolation, December 2013. URL <http://arxiv.org/abs/1302.4245>. arXiv:1302.4245 [cs, stat].
- [53] Carl Edward Rasmussen and Christopher K. I. Williams. *Gaussian processes for machine learning*. Adaptive computation and machine learning. MIT Press, Cambridge, Mass, 2006. ISBN 978-0-262-18253-9. OCLC: ocm61285753.
- [54] Ingo Steinbach. Phase-field models in materials science. *Modelling and Simulation in Materials Science and Engineering*, 17(7):073001, July 2009. ISSN 0965-0393. doi: 10.1088/0965-0393/17/7/073001. URL <https://dx.doi.org/10.1088/0965-0393/17/7/073001>.
- [55] Christian Miehe, Martina Hofacker, and Fabian Welschinger. A phase field model for rate-independent crack propagation: Robust algorithmic implementation based on operator splits. *Computer Methods in Applied Mechanics and Engineering*, 199(45):2765–2778, November 2010. ISSN 0045-7825. doi: 10.1016/j.cma.2010.04.011. URL <https://www.sciencedirect.com/science/article/pii/S0045782510001283>.
- [56] Ekkehart Kröner. *Statistical Continuum Mechanics*, volume 92 of *CISM International Centre for Mechanical Sciences*. Springer Vienna, Vienna, 1971. ISBN 978-3-211-81129-0. doi: 10.1007/978-3-7091-2862-6. URL <http://link.springer.com/10.1007/978-3-7091-2862-6>.
- [57] Salvatore Torquato. *Random Heterogeneous Materials: Microstructure and Macroscopic Properties*. Interdisciplinary Applied Mathematics. Springer-Verlag, New York, 2002. ISBN 978-0-387-95167-6. doi: 10.1007/978-1-4757-6355-3. URL <https://www.springer.com/gp/book/9780387951676>.
- [58] Valentin De Bortoli, James Thornton, Jeremy Heng, and Arnaud Doucet. Diffusion Schrödinger Bridge with Applications to Score-Based Generative Modeling, April 2023. URL <http://arxiv.org/abs/2106.01357>. arXiv:2106.01357 [cs, math, stat].

- [59] John W. Cahn and John E. Hilliard. Free Energy of a Nonuniform System. I. Interfacial Free Energy. *Journal of Chemical Physics*, 28:258–267, February 1958. ISSN 0021-9606/0301-0104. doi: 10.1063/1.1744102. URL <https://ui.adsabs.harvard.edu/abs/1958JChPh..28..258C>. ADS Bibcode: 1958JChPh..28..258C.
- [60] David Montes de Oca Zapiain, James A. Stewart, and Rémi Dingreville. Accelerating phase-field-based microstructure evolution predictions via surrogate models trained by machine learning methods. *npj Computational Materials*, 7(1):1–11, January 2021. ISSN 2057-3960. doi: 10.1038/s41524-020-00471-8. URL <https://www.nature.com/articles/s41524-020-00471-8>. Number: 1 Publisher: Nature Publishing Group.
- [61] R Dingreville, J A Stewart, and E Y Chen. Benchmark problems for the Mesoscale Multiphysics Phase Field Simulator (MEMPHIS). Technical report, April 2020.
- [62] Stephen R. Niezgoda, Yuksel C. Yabansu, and Surya R. Kalidindi. Understanding and visualizing microstructure and microstructure variance as a stochastic process. *Acta Materialia*, 59(16):6387–6400, September 2011. ISSN 1359-6454. doi: 10.1016/j.actamat.2011.06.051. URL <https://www.sciencedirect.com/science/article/pii/S1359645411004654>.
- [63] Akash Gupta, Ahmet Cecen, Sharad Goyal, Amarendra K. Singh, and Surya R. Kalidindi. Structure–property linkages using a data science approach: Application to a non-metallic inclusion/steel composite system. *Acta Materialia*, 91:239–254, June 2015. ISSN 1359-6454. doi: 10.1016/j.actamat.2015.02.045. URL <http://www.sciencedirect.com/science/article/pii/S1359645415001603>.
- [64] Marat I. Latypov, Laszlo S. Toth, and Surya R. Kalidindi. Materials knowledge system for nonlinear composites. *Computer Methods in Applied Mechanics and Engineering*, 346:180–196, April 2019. ISSN 0045-7825. doi: 10.1016/j.cma.2018.11.034. URL <http://www.sciencedirect.com/science/article/pii/S0045782518305930>.
- [65] Yuksel C. Yabansu, Patrick Altschuh, Johannes Hötzer, Michael Selzer, Britta Nestler, and Surya R. Kalidindi. A digital workflow for learning the reduced-order structure-property linkages for permeability of porous membranes. *Acta Materialia*, 195:668–680, August 2020. ISSN 1359-6454. doi: 10.1016/j.actamat.2020.06.003. URL <http://www.sciencedirect.com/science/article/pii/S1359645420304274>.
- [66] Andrew Marshall and Surya R. Kalidindi. Autonomous Development of a Machine-Learning Model for the Plastic Response of Two-Phase Composites from Micromechanical Finite Element Models. *JOM*, 73(7):2085–2095, July 2021. ISSN 1543-1851. doi: 10.1007/s11837-021-04696-w. URL <https://doi.org/10.1007/s11837-021-04696-w>.
- [67] Noah H. Paulson, Matthew W. Priddy, David L. McDowell, and Surya R. Kalidindi. Reduced-order structure-property linkages for polycrystalline microstructures based on 2-point statistics. *Acta Materialia*, 129:428–438, May 2017. ISSN 1359-6454. doi: 10.1016/j.actamat.2017.03.009. URL <http://www.sciencedirect.com/science/article/pii/S135964541730188X>.
- [68] Adam P. Generale and Surya R. Kalidindi. Reduced-order models for microstructure-sensitive effective thermal conductivity of woven ceramic matrix composites with residual porosity. *Composite Structures*, 274:114399, October 2021. ISSN 02638223. doi: 10.1016/j.compstruct.2021.114399. URL <https://linkinghub.elsevier.com/retrieve/pii/S0263822321008618>.
- [69] Surya R. Kalidindi. Feature engineering of material structure for AI-based materials knowledge systems. *Journal of Applied Physics*, 128(4):041103, July 2020. ISSN 0021-8979. doi: 10.1063/5.0011258. URL <https://aip.scitation.org/doi/10.1063/5.0011258>. Publisher: American Institute of Physics.
- [70] Grayson H. Harrington, Conlain Kelly, Vahid Attari, Raymundo Arroyave, and Surya R. Kalidindi. Application of a Chained-ANN for Learning the Process-Structure Mapping in Mg₂Si₆Sn_{1-x} Spinodal Decomposition. *Integrating Materials and Manufacturing Innovation*, 11(3):433–449, September 2022. ISSN 2193-9772. doi: 10.1007/s40192-022-00274-3. URL <https://doi.org/10.1007/s40192-022-00274-3>.
- [71] Rémi Flamary, Nicolas Courty, Alexandre Gramfort, Mokhtar Z. Alaya, Aurélie Boisbunon, Stanislas Chambon, Laetitia Chapel, Adrien Corenflos, Kilian Fatras, Nemo Fournier, Léo

- Gautheron, Nathalie T. H. Gayraud, Hicham Janati, Alain Rakotomamonjy, Ievgen Redko, Antoine Rolet, Antony Schutz, Vivien Seguy, Danica J. Sutherland, Romain Tavenard, Alexander Tong, and Titouan Vayer. POT: Python Optimal Transport. *Journal of Machine Learning Research*, 22(78):1–8, 2021. ISSN 1533-7928. URL <http://jmlr.org/papers/v22/20-451.html>.
- [72] Kilian Fatras, Younes Zine, Szymon Majewski, Rémi Flamary, Rémi Gribonval, and Nicolas Courty. Minibatch optimal transport distances; analysis and applications, January 2021. URL <http://arxiv.org/abs/2101.01792>. arXiv:2101.01792 [cs, stat].
- [73] Kilian Fatras, Younes Zine, Rémi Flamary, Rémi Gribonval, and Nicolas Courty. Learning with minibatch Wasserstein : asymptotic and gradient properties, October 2021. URL <http://arxiv.org/abs/1910.04091>. arXiv:1910.04091 [cs, stat].
- [74] Dan Hendrycks and Kevin Gimpel. Gaussian Error Linear Units (GELUs), June 2023. URL <http://arxiv.org/abs/1606.08415>. arXiv:1606.08415 [cs].
- [75] Ilya Loshchilov and Frank Hutter. Decoupled Weight Decay Regularization, January 2019. URL <http://arxiv.org/abs/1711.05101>. arXiv:1711.05101 [cs, math].
- [76] Sepp Hochreiter and Jürgen Schmidhuber. Long Short-Term Memory. *Neural Computation*, 9(8):1735–1780, November 1997. ISSN 0899-7667. doi: 10.1162/neco.1997.9.8.1735. URL <https://ieeexplore.ieee.org/abstract/document/6795963>. Conference Name: Neural Computation.

A Appendix: Proofs of Theorems

A.1 Proof $p_t(x|y)$ and $u_t(x|y)$ satisfy the continuity equation

Theorem 3.1 *The marginal conditional vector field Eq. (9) generates the marginal conditional probability path Eq. (8) from $p_0(x|y)$ given samples of $q(z, w)$ if $q(y_0) = q(y_1)$ and (x_0, y_0) and (x_1, y_1) are drawn from $q(z, w)$ following the conditional optimal coupling $\pi(y_0, y_1)$ over w .*

Proof. The continuity equation provides a necessary and sufficient condition for a vector field to generate a probability distribution [37]. Therefore, the proof is completed by demonstrating that $u_t(x|y)$, defined by Eq. (9), meets the continuity equation for the conditional distribution $p_t(x|y)$. We utilize the assumed decomposition introduced in the main body of the paper, $p(x, y|z, w) = p(x|z)p(y|w)$. Additionally, we assume that x is independent of w given y , $p_t(x|y, w) = p_t(x|y)$. Finally, we will require that $p(y_0) = p(y_1)$. In other words, that the distribution on the conditioning variable is the same at t_0 and t_1 . We argue that this is not a very restrictive requirement in practice. It is the situation that occurs in many applications, in particular scientific dynamics problems where the distribution on conditions is constant over all time.

$$\frac{d}{dt}(p_t(x|y)) = -\text{div}_x(p_t(x|y)u_t(x|y)) \quad (\text{A.1})$$

We begin with expanding the left hand side of the continuity equation in Eq. (A.1). To clarify notation, we utilize $p(\cdot)$ to denote probability density functions over the primary variables, x and y . We use $q(\cdot)$ to denote distributions over the pair variables z and w . The subscript t denotes time dependence. Their arguments differentiate the multiple distributions of each type.

$$\begin{aligned} \frac{d}{dt}(p_t(x|y)) &= \frac{d}{dt} \left(\frac{p_t(x, y)}{p_t(y)} \right) \\ &= \frac{d}{dt} \left(\int \frac{p_t(x, y|w, z)}{p_t(y)} q(w, z) dz dw \right) \end{aligned}$$

We utilize the following assumed decomposition, $p_t(x, y|w, z) = p_t(x|z)p_t(y|w)$,

$$\begin{aligned}
&= \frac{d}{dt} \left(\int \frac{p_t(x|z)p_t(y|w)}{p_t(y)} q(w, z) dz dw \right) \\
&= \int \left[\underbrace{\frac{p_t(y|w)}{p_t(y)} \frac{d}{dt} (p_t(x|z))}_{T_1} - \underbrace{\frac{p_t(x|z)p_t(y|w)}{p_t(y)^2} \frac{d}{dt} (p_t(y))}_{T_2} + \underbrace{\frac{p_t(x|z)}{p_t(y)} \frac{d}{dt} (p_t(y|w))}_{T_3} \right] q(w, z) dz dw
\end{aligned}$$

We next consider each of the individual terms above. We will extensively rely upon the fact that we have prescribed forms to $u_t(x|z)$ and $u_t(y|w)$ such that they generate $p_t(x|z)$ and $p_t(y|w)$, respectively (see Theorem 3 of Lipman et al. [17] or Theorem 2.1 in Tong et al. [14]). The integrands are further assumed to satisfy the regularity conditions of the Leibniz Rule for changing the order of integration and differentiation. Beginning with the first term, T_1 ,

$$T_1 = \int \frac{p_t(y|w)}{p_t(y)} \frac{d}{dt} (p_t(x|z)) q(w, z) dz dw$$

as $u_t(x|z)$ generates $p_t(x|z)$,

$$= - \int \frac{p_t(y|w)}{p_t(y)} \text{div}_x (p_t(x|z) u_t(x|z)) q(w, z) dz dw$$

Leibniz Rule,

$$\begin{aligned}
&= -\text{div}_x \left(\int \frac{p_t(y|w)p_t(x|z)q(w, z)}{p_t(y)} u_t(x|z) dz dw \right) \\
&= -\text{div}_x \left(p_t(x|y) \int \frac{p_t(y|w)p_t(x|z)q(w, z)}{p_t(y)p_t(x|y)} u_t(x|z) dz dw \right)
\end{aligned}$$

using the definition of $u_t(x|y)$, Eq. (9),

$$= -\text{div}_x (p_t(x|y) u_t(x|y))$$

Here, we arrive at the right hand side of the continuity equation. Next, we turn to demonstrating that terms T_2 and T_3 equate to zero. We begin inspecting the second term, T_2 ,

$$\begin{aligned}
T_2 &= \int -\frac{p_t(x|z)p_t(y|w)}{p_t(y)^2} \frac{d}{dt} (p_t(y)) q(w, z) dz dw \\
&= -\frac{1}{p_t(y)^2} \frac{d}{dt} (p_t(y)) \int p_t(x|z)p_t(y|w) q(w, z) dz dw \\
&= -\frac{p_t(x|y)}{p_t(y)} \frac{d}{dt} p_t(y)
\end{aligned}$$

Next, we consider the last term, T_3 , before returning to T_2 .

$$T_3 = \int \frac{p_t(x|z)}{p_t(y)} \frac{d}{dt} (p_t(y|w)) q(w, z) dz dw$$

as $u_t(y|w)$ generates $p_t(y|w)$,

$$= - \int \frac{p_t(x|z)}{p_t(y)} \text{div}_y (p_t(y|w) u_t(y|w)) q(w, z) dz dw$$

Leibniz Rule,

$$= - \frac{1}{p_t(y)} \text{div}_y \left(\int u_t(y|w) p_t(x|z) p_t(y|w) q(w, z) dz dw \right)$$

marginalization on z , the chain rule of probability, and the second assumption outlined previously,

$$\begin{aligned} &= - \frac{1}{p_t(y)} \text{div}_y \left(\int u_t(y|w) p_t(x|y) p_t(y|w) q(w) dw \right) \\ &= - \frac{1}{p_t(y)} \text{div}_y \left(p_t(x|y) p_t(y) \int u_t(y|w) \frac{p_t(y|w) q(w)}{p_t(y)} dw \right) \end{aligned}$$

definition of the marginal vector field, Eq. (8) in Lipman et al. [17] or Eq. (9) in Tong et al. [14]

$$= - \frac{1}{p_t(y)} \text{div}_y (p_t(x|y) p_t(y) u_t(y))$$

product rule,

$$= - \frac{1}{p_t(y)} p_t(y) u_t(y)^T \nabla_y p_t(x|y) - \frac{p_t(x|y)}{p_t(y)} \text{div}_y (p_t(y) u_t(y))$$

$u_t(y)$ generates $p_t(y)$,

$$\begin{aligned} &= - \frac{1}{p_t(y)} p_t(y) u_t(y)^T \nabla_y p_t(x|y) + \frac{p_t(x|y)}{p_t(y)} \frac{d}{dt} p_t(y) \\ &= - u_t(y)^T \nabla_y p_t(x|y) + \frac{p_t(x|y)}{p_t(y)} \frac{d}{dt} p_t(y) \end{aligned}$$

Combining T_1 , T_2 , and T_3 together, we obtain,

$$\begin{aligned} \frac{d}{dt} (p_t(x|y)) &= T_1 + T_2 + T_3 \\ &= - \text{div}_x (p_t(x|y) u_t(x|y)) - \frac{p_t(x|y)}{p_t(y)} \frac{d}{dt} p_t(y) - u_t(y)^T \nabla_y p_t(x|y) + \frac{p_t(x|y)}{p_t(y)} \frac{d}{dt} p_t(y) \\ &= - \text{div}_x (p_t(x|y) u_t(x|y)) - u_t(y)^T \nabla_y p_t(x|y) \end{aligned}$$

Optimal Transport between $q(y_0) = q(y_1)$: The continuity equation is left with $-u_t(y)^T \nabla_y p_t(x|y)$. In general, this remainder is nonzero. For arbitrary empirical distributions $q(x_0, y_0)$ and $q(x_1, y_1)$, the $u_t(x|y)$ defined by Eq. (9) generates $p_t(x|y)$ only if the flow over y is carefully designed, such that it is orthogonal to $\nabla_y p_t(x|y)$ for all t .

In fact, in the problem settings discussed in this paper and under the proposed CVFM training scheme, we are in one of these rare situations. Consider our final assumption: $q(y_0) = q(y_1)$. In other words, we assume that the underlying distributions – represented by the empirical set of observations – of the conditioning variables at the boundary times are equivalent. Importantly, the set of samples representing each distribution implicitly are not equal. Additionally, the set sizes can be imbalanced. When $q(y_0) = q(y_1)$, the optimal transport flow does nothing, resulting in

$dp_t(y)/dt = 0$ and $u_t(y) = 0$. Importantly, in CVFM, we only utilize a conditional flow, $u_t(y|w)$, which approximates the flow over y , $u_t(y)$, in expectation. In general, this type of conditional approximation is not guaranteed to produce the marginal optimal transport map. However, when static optimal transport is utilized in training, Tong et al. [1], Pooladian et al. [41] show that this results in the expectation of the conditional flow sufficiently approximating the marginal OT.

In fact, we directly observed the impact of mini-batch OT (and the scaling kernel) and this remainder in the first presented case study. Without mini-batch OT, the learned $u_t(x|y)$ cannot generate the required marginal conditional vector field generating $p_t(x|y)$. Only once conditional optimal transport was incorporated could the appropriate push-forward operation be obtained. Importantly, this behavior differs from previous flow matching efforts where learning the appropriate vector field is possible with or without optimal transport [1, 19, 41, 50].

Therefore, because $q(y_0) = q(y_1)$ and static optimal transport is used in training, Section 3.3, the remainder disappears and $u_t(x|y)$ defined by Eq. (9) and $p_t(x|y)$ satisfy the continuity equation.

$$\begin{aligned} \frac{d}{dt}(p_t(x|y)) &= -\text{div}_x(p_t(x|y)u_t(x|y)) - \underbrace{u_t(y)}_{\rightarrow 0} \nabla_y p_t(x|y) \\ &= -\text{div}_x(p_t(x|y)u_t(x|y)) \end{aligned} \quad (\text{A.2})$$

A.2 Equivalence of the Flow Matching Objective

Theorem 3.2 *If $p_t(x|y) > 0$ for all $x \in \mathbb{R}^N$ and for all $y \in \mathbb{R}^M$ and $t \in [0, 1]$, then, $\mathcal{L}_{\text{MCFM}}(\theta)$ (r.h.s. below) and $\mathcal{L}_{\text{CVFM}}(\theta)$ are equal up to a constant, and hence:*

$$\nabla_\theta \mathcal{L}_{\text{CVFM}}(\theta) = \nabla_\theta \mathbb{E}_{t, p_t(x, y)} \|v_\theta(x, y, t) - u_t(x|y)\|^2 \quad (\text{A.3})$$

Proof. As in Lipman et al. [17], several assumptions are necessary to guarantee the existence of various integrals and to allow exchanging of their order. Specifically, we assume $q(w, z)$, $p_t(x|z)$, $p_t(y|w)$ and $p(w)$ decrease to zero as $\|x\|, \|y\| \rightarrow \infty$ and that v_t , v_t , and $\nabla_\theta v_t$ are bounded. Furthermore, the optimal transport penalty, η , is taken to be sufficiently large such that when sampling in mini-batches approximating the optimal coupling between $q(y_0)$ and $q(y_1)$, $y_0 \approx y_1$. Additionally, we assume that $\alpha(w)$ is sufficiently differentiable to be approximated using a Taylor series. Under these conditions, $\alpha(w) = \alpha(\|y_0 - y_1\|_2)$ is well approximated by Taylor series centered at zero.

We begin by stating the intractable marginal conditional flow matching (MCFM) objective

$$\mathcal{L}_{\text{MCFM}}(\theta) = \mathbb{E}_{t, p_t(x, y)} \|v_\theta(x, y, t) - u_t(x|y)\|^2 \quad (\text{A.4})$$

Expanding the L_2 -norm

$$\begin{aligned} \mathcal{L}_{\text{MCFM}}(\theta) &= \mathbb{E}_{t, p_t(x, y)} \|v_\theta(x, y, t) - u_t(x|y)\|^2 \\ &= \mathbb{E}_{t, p_t(x, y)} \left[\underbrace{\|v_\theta(x, y, t)\|^2}_{T_1} - 2 \underbrace{\langle v_\theta(x, y, t), u_t(x|y) \rangle}_{T_1} + \underbrace{\|u_t(x|y)\|^2}_{T_3} \right] \end{aligned}$$

Consider each term independently. Note, the third term can be ignored because it is independent of the trainable parameters.

$$\begin{aligned} T_1 &= \mathbb{E}_{t, p_t(x, y)} [\|v_\theta(x, y, t)\|^2] \\ &= \mathbb{E}_t \left[\int p_t(x, y, w, z) \|v_\theta(x, y, t)\|^2 dz dw dx dy \right] \\ &= \mathbb{E}_t \left[\int p_t(x|z) p_t(y|w) q(z, w) \|v_\theta(x, y, t)\|^2 dz dw dx dy \right] \\ &= \mathbb{E}_{t, p_t(x|z), p_t(y|w), q(z, w)} [\|v_\theta(x, y, t)\|^2] \end{aligned}$$

Consider the second term.

$$\begin{aligned}
T_2 &= -2\mathbb{E}_{t,p_t(x,y)} [\langle v_\theta(x,y,t), u_t(x|y) \rangle] \\
&= -2\mathbb{E}_t \left[\int p_t(x,y) \left\langle v_\theta(x,y,t), \int u_t(x|z) \frac{p_t(x,y|z,w)q(z,w)}{p_t(x,y)} dz dw \right\rangle dx dy \right] \\
&= -2\mathbb{E}_t \left[\int p_t(x,y) \frac{p_t(x,y|z,w)q(z,w)}{p_t(x,y)} \langle v_\theta(x,y,t), u_t(x|z) \rangle dx dy dz dw \right] \\
&= -2\mathbb{E}_t \left[\int p_t(x|z)p_t(y|z)q(z,w) \langle v_\theta(x,y,t), u_t(x|z) \rangle dx dy dz dw \right] \\
&= -2\mathbb{E}_{t,p_t(x|z),p_t(y|z),q(z,w)} [\langle v_\theta(x,y,t), u_t(x|z) \rangle]
\end{aligned}$$

Combining these together and comparing them against the expanded form for $\mathcal{L}_{\text{CVFM}}(\theta)$, we clearly see that the $\mathcal{L}_{\text{MCFM}}(\theta)$ and $\mathcal{L}_{\text{CVFM}}(\theta)$ objectives are equivalent up until a constant independent of the training parameters, θ .

The above equivalence holds directly when $\mathcal{L}_{\text{CVFM}}$ doesn't contain the scaling kernel, $\alpha(w)$. We now analyze the impact of incorporating the kernel on the derived equality and demonstrate that the equality holds to first order for the proposed exponential form.

After incorporating the kernel, the above equality remains true if the following expression holds for arbitrary choice of $f(w)$ (for example, $f(w) = \|v_\theta(x,y,t)\|^2$ in T_1).

$$\mathbb{E}_{q(w)} [f(w)] = \mathbb{E}_{q(w)} [\alpha(w)f(w)] \quad (\text{A.5})$$

Clearly, this holds exactly only if $\alpha(w) = 1$. However, under other conditions it holds to sufficient order that training remains stable. Via Taylor series analysis, $\alpha(w)$ is approximated to second order as follows. Here, for simplicity, we override the definition of w and define $w = \|y_0 - y_1\|_2$.

$$\alpha(w) \approx a(0) + C_1 \frac{\partial \alpha}{\partial w} \big|_{w=0} w + C_2 \frac{\partial^2 \alpha}{\partial w^2} \big|_{w=0} w^2 \quad (\text{A.6})$$

For $\alpha(w) = \exp(-w^2)/2\sigma_y^2$, the first term is equal to 1 and the second term is equal to 0. Only the third term remains non-zero and non-constant. Therefore, for the squared-exponential choice of $\alpha(w)$, the loss equality holds to first order. Empirically, we observe that this is sufficient for stable training even in high dimensions. A more precise analysis of the degree of agreement necessary and the optimal kernel design is left to future work.

A.3 Continuity Across Conditional Vector Fields

Theorem 3.3 *If $v_\theta(x,y,t)$ is locally Lipschitz continuous, $p_t(y|w), p_t(x|z) \in \mathcal{C}^\infty$, and $\mathcal{L}_{\text{CVFM}}(\theta)$ is continuous and differentiable with respect to y , then the learned network $v_\theta(x,y,t)$ generates conditional probability paths across the conditional Wasserstein density manifold.*

Proof. By the composition theorem, the composition of continuous functions results in a function which is similarly continuous.

We begin with the empirical distribution $q(z,w)$, which as a finite sum of Dirac delta functions is itself not inherently continuous, although expectations taken with respect to $q(z,w)$ are. Also by construction $p_t(y|w), p_t(x|z)$ are smooth and continuous distributions. $\mathcal{L}_{\text{CVFM}}(\theta)$ (Eq. (2)) is a continuous function of $v_\theta(x,y,t)$, $\alpha(w)$, and $u_t(x|z)$ by which expectations over $q(z,w), p_t(y|w), p_t(x|z)$ maintain this property.

Empirical samples are drawn according to the OT coupling $\pi(z,w)$, minimizing the ground cost defined in Eq. (12), and inducing a gradient flow in the Wasserstein sense. Section A.1 previously established adherence to the continuity equation.

Therefore, the learned network $v_\theta(x,y,t)$ results in a continuous vector field across y , generating $p_t(x|y)$ which respects the underlying geometry of the Wasserstein density space.

B Appendix: Additional Simulation-Free Score and Flow Matching Background

Tong et al. [1] proposed a simulation-free training objective for approximating continuous time Schrodinger bridges [2, 58], generalizing Flow Matching (FM) [17, 18] to the case of stochastic dynamics with arbitrary source distributions. Let $p : [0, 1] \times \mathbb{R}^N \rightarrow \mathbb{R}^+$ define a time-dependent probability path, $u : [0, 1] \times \mathbb{R}^N \rightarrow \mathbb{R}^N$ a time-dependent vector field, and $g : [0, 1] \rightarrow \mathbb{R}_{>0}$ a continuous positive diffusion function. An associated Itô stochastic differential equation (SDE) can be defined

$$dx = u_t(x)dt + g(t)dw_t \quad (\text{B.1})$$

where $u_t(x)$ is equivalent to $u(t, x)$, and dw_t is standard Brownian motion. Utilizing the *Fokker-Planck equation* and *continuity equation*, it is possible to derive the *probability flow* ordinary differential equation (ODE) of the process [1, 16] and comprise a relation between the probability flow ODE $\hat{u}_t(x)$ and the SDE drift as

$$u_t(x) = \hat{u}_t(x) + \frac{g^2(t)}{2} \nabla \log p_t(x). \quad (\text{B.2})$$

As long as the probability flow ODE and score function can be specified, the SDE can be adequately described. Tong et al. [1] demonstrated that the intuition underpinning Eq. (8) can also be extended to the marginalization over conditional scores, resulting in the expressions

$$\begin{aligned} \hat{u}_t(x) &= \int \hat{u}_t(x|z) \frac{p_t(x|z)q(z)}{p_t(x)} dz \\ \nabla \log p_t(x) &= \int \nabla \log p_t(x|z) \frac{p_t(x|z)q(z)}{p_t(x)} dz. \end{aligned} \quad (\text{B.3})$$

Gaussian marginal conditional flows: Prior works (Theorem 3 [17], Theorem 2.1 [14], Theorem 2.6, [18]) have demonstrated a method for tractably evaluating Eq. (B.3) in the case where the ODE/SDE conditional flows are Gaussian (i.e., $p_t(x|z) = \mathcal{N}(x; \mu_t(z), \sigma_t^2(z))$). The unique vector field $\hat{u}_t(x|z)$ generating this flow has the form

$$\hat{u}_t(x|z) = \frac{\sigma'_t(z)}{\sigma_t(z)}(x - \mu_t(z)) + \mu'_t(z) \quad (\text{B.4})$$

where $\sigma'_t(z)$ and $\mu'_t(z)$ denote the time derivatives of $\sigma_t(z)$ and $\mu_t(z)$, respectively. This can seamlessly be extended to define the conditional score $\nabla \log p_t(x|z) = -(x - \mu_t(z))/\sigma_t^2(z)$. In the particular case of a *Brownian bridge* from x_0 to x_1 , sampled from $q(z)$, with constant diffusion rate $g(t) = \sigma$, the conditional flow is defined as $p_t(x|z) = \mathcal{N}(x; tx_1 + (1-t)x_0, \sigma^2 t(1-t))$, resulting in

$$\begin{aligned} \hat{u}_t(x|z) &= \frac{1-2t}{t(1-t)}(x - (tx_1 + (1-t)x_0)) + (x_1 - x_0) \\ \nabla \log p_t(x|z) &= \frac{tx_1 + (1-t)x_0 - x}{\sigma^2 t(1-t)}. \end{aligned} \quad (\text{B.5})$$

In a similar manner to the derivation shown in Appendix A, a density over initial conditions $p(x_0)$, induces marginal distributions $p_t(x)$ satisfying the *Fokker-Planck equation* where $\Delta p_t = \nabla \cdot (\nabla p_t)$ [1]:

$$\frac{\partial p}{\partial t} = -\nabla \cdot (p_t u_t) + \frac{g^2(t)}{2} \Delta p_t \quad (\text{B.6})$$

In total, Tong et al. [1] demonstrate that the concept of regressing upon the conditional vector field from FM can be extended to regressing upon conditional drift and score, providing improved performance in practice.

Weighting schedule $\lambda(t)$: In the case with conditional Gaussian $p_t(x|z)$ probability paths, as in Eq. (B.4), Tong et al. [1] advocate a particular weighting schedule $\lambda(t)$:

$$\lambda(t) = \frac{2\sigma_t}{\sigma^2} = \frac{2\sqrt{t(1-t)}}{\sigma}. \quad (\text{B.7})$$

This weighting schedule provides simplification to the objective alongside numerical stability, converting the score matching objective to

$$\lambda(t)^2 \|s_\theta(x, t) - \nabla_x \log p_t(x|z)\|^2 = \|\lambda(t)s_\theta(x, t) + \varepsilon\|^2 \quad (\text{B.8})$$

where $\varepsilon \sim \mathcal{N}(0, 1)$.

C Appendix: Case Study Background

C.1 Microstructure Evolution in Materials Informatics

In this section, we provide a brief background of relevant topics for the third case study, describing relevant materials background at a high level. Appendix D and Appendix E provide more details on the datasets and empirical distributions involved in training as well as greater analysis of the case study results.

Phase-Field modeling: Phase-field simulations are commonly applied to model a number of manufacturing processes involving evolving interfaces (such as solidification/melting, spinodal decomposition, grain growth, recrystallization, and crack propagation [54, 55]). In particular, the Cahn-Hilliard equation is frequently used to describe spinodal decomposition, a spontaneous thermodynamic-instability-induced phase separation [59]. This partial differential equation models a diffusion driven process which minimizes the total energy of the system by inducing phase separation. In this work, we use the formulation described in Montes de Oca Zapiain et al. [60]; we use the standard Cahn-Hilliard equation with a double well potential describing the local contribution to the total energy [61]. The material state is represented using a single, continuous field variable, $c(x)$, that separates into two phases ($c = -1$ and $c = 1$).

$$\frac{\partial c}{\partial t} = \nabla \cdot \left(\mathcal{M}(c) \nabla \frac{\partial f(c)}{\partial c} - \kappa \nabla^2 c \right) \quad (\text{C.1a})$$

$$f(c) = \omega(c - 1)^2(c + 1)^2 \quad (\text{C.1b})$$

$$\mathcal{M}(c) = s(c)\mathcal{M}_1 + (1 - s(c))\mathcal{M}_2 \quad (\text{C.1c})$$

$$s(c) = \frac{1}{4}(2 - c)(1 + c)^2 \quad (\text{C.1d})$$

The values of the c field corresponding to each separated phase are defined by the minima of the chemical free energy density, $f(c)$. The spatially-dependent concentration field, $c(x)$, will take the role of material microstructure. The concentration dependent mobility, $\mathcal{M}(c)$, which defines the diffusion dynamics of the concentration field, $c(x)$, is parameterized by \mathcal{M}_1 and \mathcal{M}_2 which are scalar constant mobility parameters for each phase. Parameters ω and κ , the energy barrier height and the gradient energy coefficient, respectively, are both set to 1. For the purpose of modeling the system's stochastic dynamics using CVFM, the neural network is conditioned on three parameters: $\log(\mathcal{M}_1)$, $\log(\mathcal{M}_2)$, and c_0 – the initial concentration of the c field at time zero. We note that at time zero, $c(x) = c_0 + \epsilon(x)$, where $\epsilon(x)$ is a low variance, clipped white noise field (i.e., values cannot exceed $[-1, 1]$ after the sum) (e.g., $\text{STD}[\epsilon(x)] = 0.35$). This stochasticity is necessary to initiate phase separation and results in a distribution of final microstructures when a single set of

$\mathcal{M}_1, \mathcal{M}_2, c_0$ are rerun several times. The dataset utilized in this paper’s third presented case study was simulated under periodic boundary conditions using the MEMPHIS code base from Sandia National Labs [61]. Details on the dataset are included in Appendix D.6.

2-Point spatial correlations: This work uses 2-point spatial correlations [6, 7, 57] as descriptive microstructure features to quantify the state of the material microstructure at a given time. This featurization builds on the idea that the microstructure itself is a stochastic function, where individual observed microstructure instances are simply samples from governing stochastic microstructure function (SMF) [56, 57, 62]. This concept was developed and is used to account for the observed degeneracy in material microstructures represented in direct space (e.g., for spinodal decomposition, represented directly as the concentration field, $c(x)$). This degeneracy refers to the observation that visually dissimilar microstructures sampled from the same underlying SMF are characterized by identical physical properties and process evolution in response to an applied environment. Therefore, it is more physically relevant (and computationally simple) to quantify evolution in SMFs than individual observed microstructures. Within this conceptualization, the underlying stochastic microstructure function is identified from individual instances by empirically estimating the moments of the SMF – e.g., its second order moments: the 2-point statistics. In practice, it is generally sufficient to represent material microstructures using their 2-point statistics. In addition to addressing degeneracy, a 2-point statistics based representation also provides a convenient mechanism to account for underlying symmetries (such as translation-equivariance and periodicity).

In practice, 2-point spatial correlations can be computed as a convolution of the sampled discrete microstructure function m_s^α , where α indexes the material local state and s indexes the spatial voxel. For the considered spinodal decomposition problem, $m_s = c_s$ has a one dimensional state. The resulting 2-point spatial correlations between two arbitrary material states, α and β , are then defined by the operation

$$f_r^{\alpha\beta} = \frac{1}{S} \sum_{s=1}^S m_s^\alpha m_{s+r}^\beta \quad (\text{C.2})$$

where S is the number of voxels in the microstructural domain. Dimensionality reduction techniques can then be effectively applied to a dataset of 2-point spatial correlations to provide robust, information-dense features for the construction of linkages between process parameters and internal material structure [63–70].

D Appendix: Experimental Details

D.1 Algorithm

In this section, we present the general algorithm for Conditional Variable Flow Matching given $q(z, w)$, $p_t(x|z)$, $p_t(y|w)$, and $u_t(x|z)$ in Algorithm 1, and the Schrödinger bridge extension with flow and score matching given $\nabla_x \log p_t(x|z)$ in Algorithm 2.

D.2 Static Optimal Transport

Static exact and entropic regularized optimal transport couplings were solved for in mini-batches during training through the Python Optimal Transport (POT) package [71] (<https://pythonot.github.io/>). As similarly reported in [1], we noticed improved performance in the low-dimensional toy cases with the Sinkhorn algorithm [38], which degraded in higher dimensions (e.g., material dynamics, domain transfer). The use of mini-batch optimal transport has also been previously shown to regularize the transport plan [72, 73] due to the stochastic nature of the independent batch samplings forming non-optimal couplings, in effect resulting in entropic-regularized OT plans, even with exact OT solves.

Algorithm 1 Conditional Variable Flow Matching

Require: Source and target data distributions $q(x_0, y_0)$ and $q(x_1, y_1)$ consisting of two unpaired sets of observed samples, noise hyperparameters σ_x, σ_y , mini-batch size B , and network v_θ .

while Training **do**

$\{(x_0, y_0), (x_1, y_1)\}_{b=1}^B \sim q(x_0, y_0), q(x_1, y_1)$ \triangleright Sample empirical distributions of size B .

$\pi \leftarrow \text{OT}(\{(x_0, y_0), (x_1, y_1)\}_{b=1}^B)$ \triangleright Interchangeable with Sinkhorn algorithm [38].

$t \sim \mathcal{U}(0, 1)$

$\{(x_0, x_1), (y_0, y_1)\}_{b=1}^B \sim \pi(z, w)$ \triangleright Resample from OT coupling.

$z = [(x_0^{(1)}, x_1^{(1)}), \dots, (x_0^{(B)}, x_1^{(B)})], \quad w = [(y_0^{(1)}, y_1^{(1)}), \dots, (y_0^{(B)}, y_1^{(B)})]$

$\alpha(w) \leftarrow \exp(-\|y_0 - y_1\|_2^2 / 2\sigma_y^2)$ \triangleright Evaluate kernel for sampled conditioning values.

$p_t(x|z) \leftarrow \mathcal{N}(x; tx_1 + (1-t)x_0, \sigma_x^2)$

$p_t(y|w) \leftarrow \mathcal{N}(y; ty_1 + (1-t)y_0, \sigma_y^2)$

$x_t \sim p_t(x|z)$

$y_t \sim p_t(y|w)$

$u_t(x|z) \leftarrow x_1 - x_0$

$\mathcal{L}_{\text{CVFM}}(\theta) \leftarrow \mathbb{E}_{t, q(z, w), p_t(x, y|z, w)} [\alpha(w) \|v_\theta(x, y, t) - u_t(x|z)\|^2]$

$\theta \leftarrow \text{Update}(\theta, \nabla_\theta \mathcal{L}_{\text{CVFM}}(\theta))$

end while

return v_θ

Algorithm 2 Conditional Variable Score and Flow Matching

Require: Source and target data distributions $q(x_0, y_0)$ and $q(x_1, y_1)$ consisting of two unpaired sets of observed samples, noise hyperparameters σ_x, σ_y , mini-batch size B , weighting schedule $\lambda(t)$, drift network v_θ , and score network s_θ .

while Training **do**

$\{(x_0, y_0), (x_1, y_1)\}_{b=1}^B \sim q(x_0, y_0), q(x_1, y_1)$ \triangleright Sample empirical distributions of size B .

$\pi \leftarrow \text{Sinkhorn}(\{(x_0, y_0), (x_1, y_1)\}_{b=1}^B, 2\sigma_x^2)$

$t \sim \mathcal{U}(0, 1)$

$\{(x_0, x_1), (y_0, y_1)\}_{b=1}^B \sim \pi(z, w)$ \triangleright Resample from OT coupling.

$z = [(x_0^{(1)}, x_1^{(1)}), \dots, (x_0^{(B)}, x_1^{(B)})], \quad w = [(y_0^{(1)}, y_1^{(1)}), \dots, (y_0^{(B)}, y_1^{(B)})]$

$\alpha(w) \leftarrow \exp(-\|y_0 - y_1\|_2^2 / 2\sigma_y^2)$ \triangleright Evaluate kernel for sampled conditioning values.

$p_t(x|z) \leftarrow \mathcal{N}(x; tx_1 + (1-t)x_0, \sigma_x^2)$

$p_t(y|w) \leftarrow \mathcal{N}(y; ty_1 + (1-t)y_0, \sigma_y^2)$

$x_t \sim p_t(x|z)$

$y_t \sim p_t(y|w)$

$u_t(x|z) \leftarrow ((1-2t)/(2t(1-t)))(x - (tx_1 + (1-t)x_0)) + (x_1 - x_0)$

$\nabla_x \log p_t(x|z) \leftarrow (tx_1 + (1-t)x_0 - x)/(\sigma_x^2 t(1-t))$

$\mathcal{L}_{\text{CVSFM}}(\theta) \leftarrow \mathbb{E}_{t, q(z, w), p_t(x, y|z, w)} [\alpha(w) (\|v_\theta(x, y, t) - u_t(x|z)\|^2 + \lambda(t)^2 \|s_\theta(x, y, t) - \nabla_x \log p_t(x|z)\|^2)]$

$\theta \leftarrow \text{Update}(\theta, \nabla_\theta \mathcal{L}_{\text{CVSFM}}(\theta))$

end while

return v_θ, s_θ

D.3 Computational Resources

All experiments were performed on a high-performance-computing cluster with CPU nodes of 24 CPUs and GPU nodes with V100 and A100 GPUs. 2D experiments were all performed on 1 V100, domain transfer and material dynamics experiments were performed on 4x V100's or 2x A100's.

D.4 2D Experimental Details

The 2D experiments involve three toy examples: 8 Gaussians-Moons, 8 Gaussians-8 Gaussians, and Moons-Moons. These simple case studies are meant to analyze the training stability of CVFM

(and ablations of CVFM), baseline CVFM’s performance against alternative solutions, and provide a sufficiently low-dimensional setting to visualize and analyze the flow pathways. The next paragraphs detail the data generation process for the toy case studies. For all three, mini-batches were generated on the fly from new samples from the base distributions. In Figure E.1, the source distributions are labeled with blue samples and the target distributions are labeled with red samples. We refer the reader to the linked github code for the exact implementation.

The 8 Gaussians-Moons toy problem involves discrete conditioning that can take 8 individual values. Each condition value uniquely identifies one of the 8 Gaussians. The probability of each condition value was uniform. The two moons are each separated into 4 corresponding sections each. Each moon was separated by assigning a given sample to a select condition value dictated by the sample’s relative angle with respect to the origin of the containing moon. Each moon was broken into 4 condition value groups based on 45° degree segments. As shown in Figure E.1, the individual Gaussians share condition value with a specific moon in an alternating pattern. This leads to a flow with greater bifurcations. During training, new samples are generated for each mini-batch. Samples from the 8-Gaussians and the moons (including both x -location in 2D space and condition value, y) are generated independently to construct a mini-batch sampling from $q_{\text{Gauss}}(x_0, y_0)$ and $q_{\text{moon}}(x_1, y_1)$.

The 8 Gaussians-8 Gaussians toy problem also involves discrete conditioning that can take 8 unique values. The probability of each condition value was uniform. Each set of Gaussians is arranged in a circle, Fig. E.1. A single unique condition value is assigned to each Gaussian in a given set. The condition value assignments for each set are offset from each other by a single place rotation. Empirically, we observed that the proximity of the two rings leads to a flow with strong coupling between x and y that is challenging to learn. Samples are generated on the fly in each mini-batch. Each ring is sampled independently (first the Gaussian index is sampled, and then x -coordinates are sampled). The outer ring is the source distribution: $q_{\text{outer}}(x_0, y_0)$ and $q_{\text{inner}}(x_1, y_1)$.

Finally, the Moons-Moons toy problem involves continuous conditioning. As shown in Figure E.1, the red target moons are rotated 90° degrees with respect to the blue source moons. The rotation is performed about the combined origin of the two moons in the source distribution. Continuous conditioning is assigned based on the absolute location of a sample. The same expression is used for both the source and target distributions: $y = (x_0 - 10)I_{[0,1]} + (1 - I_{[0,1]})(x_0 + 10)$. Here, x_0 refers to the 0 component of the 2D x (not x at time 0 as has been used in the rest of the paper). $I_{[0,1]}$ denotes a binary indicator denoting which moon in the pair the sample came from. To generate the target distribution, samples are drawn from the source. Then, the sample conditional label is assigned based on the reported equation. The probability of each condition was defined implicitly by the sampling process. Finally, the samples are rotated 90° degree. Via these operations, samples within the mini-batch are drawn independently from distributions $q_{M1}(x_0, y_0)$ and $q_{M2}(x_1, y_1)$.

For all 2D synthetic dataset cases we used networks of four layers with width 128 and GELU activations [74]. Optimization was carried out with a constant learning rate of $1e-3$ and ADAM-W [75] over 10,000 steps and a batch size of 256, unless otherwise specified. Sampling was performed by integration with the adaptive step size `dopri5` solver and tolerances `atol` = `rtol` = $1e-5$. Conditional probability paths $p_t(x|z)$ were defined with $\sigma_x = 0.1$, which was held constant throughout all cases. Values of η and σ_y for $p_t(y|w)$ were varied between discrete and continuous conditioning cases. In discrete conditioning cases (8 *Gaussian* - 8 *Gaussian* and 8 *Gaussian* - *Moons*), $\sigma_y = 0.02$ and $\eta = 100$, whereas in the continuous conditioning case (*Moons* - *Moons*), $\sigma_y = 0.5$ and $\eta = 5$.

Empirical values of the Wasserstein-2 distance were evaluated through 2,048 samples simulated through the learned conditional vector fields and computed against an equivalent number of samples from the target distribution. The W_2 reported distance differs depending on cases with continuous or discrete conditioning. In the discrete case, we take the mean of the conventional W_2 distance across all conditioning classes

$$W_2(\hat{p}_1, q_1) = \mathbb{E}_{y \sim p(y)} \left[\left(\inf_{\pi \in \Pi(\hat{p}_1, q_1)} \int \|x_i - x_j\|^2 d\pi(x_i, x_j) \right)^{1/2} \right] \quad (\text{D.1})$$

while in the continuous case, we incorporate the conditional ground cost as

$$W_2(\hat{p}_1, q_1) = \left(\inf_{\pi \in \Pi(\hat{p}_1, q_1)} \int [\|x_i - x_j\|^2 + \eta \|y_i - y_j\|^2] d\pi((x_i, y_i), (x_j, y_j)) \right)^{1/2} \quad (\text{D.2})$$

with $\eta = 1e5$. Both distances are computed between samples from the target distribution q_1 , and samples from q_0 simulated forward to $t = 1$ as \hat{p}_1 .

Similar to [1, 14] and [35], we also report the normalized path energy with a similar continuous/discrete split, either as the expected value across all classes in the discrete case, or with the cost as in Eq. (12). For brevity, we only repeat the normalized path energy with this latter formulation

$$\text{NPE}(q_0, \hat{p}_1) = \frac{|\mathbb{E}_{q_0(z, w)} \int \|v_\theta(x, y, t)\|^2 dt - W_2^2(q_0, \hat{p}_1)|}{W_2^2(q_0, \hat{p}_1)}. \quad (\text{D.3})$$

This quantity provides a normalized measure for the deviation of the path energy learned by the model v_θ to that which would be optimal, equivalent to the squared Wasserstein-2 distance denoting constant velocity trajectories.

D.5 MNIST-FashionMNIST Experimental Details

The second case study analyzes the performance of CVFM on high dimensional problems. In particular, it analyzes whether training remains stable when using the scaling kernel, $\alpha(w)$, on high dimensional problems (see Appendix A for theoretical analysis of the scaling kernel $\alpha(w)$). In fact, we see that training stability improves – mirroring the conclusions from the toy examples – even for the high-dimensional setting. In this case study, we explore conditional domain transfer between the MNIST and FashionMNIST datasets. This is a discrete condition problem. Here, the goal is to map samples with a given condition in the MNIST dataset to samples with the same condition in the FashionMNIST dataset. As in every case study, independent empirical distributions represent the source and target distributions. In this case study, the source distribution is the MNIST dataset where x_0 are images and y_0 are digit assignments. Similarly, x_1 and y_1 are the images and class assignments in the FashionMNIST dataset. Before Mini-batch OT Coupling, samples are drawn independently from each marginal distribution.

The MNIST-FashionMNIST domain transfer experiments utilized a UNet architecture developed by OpenAI (<https://github.com/openai/guided-diffusion/tree/main>). The network configuration utilized in this work consisted of 64 channels, with channel multiples of [1,2,2,2]. 4 heads of self-attention over 16 and 8 resolution were applied with 2 residual blocks. Optimization was carried out with cosine annealing of the learning rate from $1e - 4$ to $1e - 8$ and ADAM-W [75] with weight decay $1e - 4$ for ranges of 3,750 - 10,000 epochs and batch size of 1024, or equivalently 220,000 - 590,000 steps. Conditional probability paths were constructed with $\sigma_x = 0.1$, $\sigma_y = 1e - 3$, and mini-batch conditional OT was performed with $\eta = 10$ and $\eta = 1000$.

Unconditional FID scores (i.e., FID scores computed over the marginal distribution on x_1 to compare the target ground truth and the predicted target) were computed over 10,000 samples using *Clean-FID* (<https://github.com/GaParmar/clean-fid>). Conditional FID scores were computed using the same algorithm, however the calculation was restricted to a subset of the total samples with matching conditioning (1,000 samples per class). This methodology directly captures the distributional match in a conditional sense, with ground truth target samples corresponding to a given condition are compared against samples from the source distribution with the same condition that had been evolved through time using the learned network. LPIPS scores were computed using *torchmetrics* (<https://github.com/Lightning-AI/torchmetrics>).

D.6 Material Dynamics Experimental Details

The final case study analyzes the performance of the proposed CVFM algorithm on our target scientific application: modeling the stochastic dynamics of a materials manufacturing process. Unlike the previous examples, the time variable now represents real time in the manufacturing process. In addition, the learned flow passes through a long sequence of empirical intermediate distributions instead of just two boundary distributions.

We use a dataset generated via spinodal decomposition simulations in MEMPHIS [61], see Appendix C. The dataset contains simulations of the evolution pathway (i.e., trajectory) of 10,000 two-phase microstructures of size 256×256 pixels. Each simulation is associated with mobility parameters \mathcal{M}_1 and \mathcal{M}_2 , sampled according to the log-uniform $\log(\mathcal{M}) \sim \mathcal{U}(\log(0.1), \log(100))$, and an initial concentration $c_0 \sim \mathcal{U}(-0.7, 0.7)$. These processing parameters correspond to the mobility parameters of the two constituents ($\mathcal{M}_1, \mathcal{M}_2$), and initial relative concentrations (c_0). Each microstructure’s trajectory contains 100 sequential recorded frames representing the microstructure state at a given time (therefore, there are 1M total microstructures spanning 100 time steps). The dataset is split into 8,000 training trajectories and 2,000 testing trajectories. The microstructure state at any given time was represented using principal component-based dimensionality reduction of the 2-point statistics, Appendix C. The Principal Component Analysis basis was established based on the complete training dataset. All models were trained to evolve the coefficients of the first 5 PC dimensions.

We note that while complete trajectories for a given $(\mathcal{M}_1, \mathcal{M}_2, c_0)$ are available (and, therefore, paired data is available), the paired data is not utilized in training in order to simulate expected conditions in envisioned experimental applications. The complete trajectories are only used to compute error metrics in testing and to compare against standard methods (such as Neural ODE [36] and LSTM [76]) that require paired data for training. Instead, state and conditioning pairs are randomly shuffled within each recorded frame in the dataset. They are combined together into joint distributions conditioned on time, $q_{mat}(x, y|\tau)$. Here, x is the PC coefficients representing the microstructure state. $y = (\log(\mathcal{M}_1), \log(\mathcal{M}_2), c_0)$ is the condition vector containing the mobilities and initial concentrations. τ is the absolute time of the sampled frame. For our example, this empirical distribution contains 800,000 sample triplets. During training, minor adjustments are made to the underlying CVSFM algorithm (Algorithm 2) to account for the presence of multiple discrete time marginal distributions. Specifically, within each step we first sample a tuple of adjacent time pairs $(\tau_0, \tau_1) \sim \{(\tau_i, \tau_{i+1})\}_{i=0}^{T=99}$. Given this time pair, a mini-batch of size $2B$ (x, y) tuple is drawn for each of these adjacent times. Each time-adjacent mini-batch is then resampled according to the empirical OT map (i.e., samples are drawn from the mini-batch estimate of the optimal coupling). Lastly, The standard CVFM algorithm is adjusted such that $t \sim \mathcal{U}(0, 1)$ and then linearly mapped to $\tau = \tau_0 + t(\tau_1 - \tau_0)$ where $\tau \in [\tau_0, \tau_1]$. This complete CVSFM algorithm for stochastic dynamics is outlined in Algorithm 3.

Algorithm 3 Time-Specific Conditional Variable Score and Flow Matching for Stochastic Dynamics

Require: Source and target data distributions $q(x_0, y_0)$ and $q(x_1, y_1)$ consisting of two unpaired sets of observed samples, noise hyperparameters σ_x, σ_y , mini-batch size B , weighting schedule $\lambda(t)$, drift network v_θ , and score network s_θ .

while Training **do**

$(\tau_0, \tau_1) \sim \{(\tau_i, \tau_{i+1})\}_{i=0}^{T=99}$ ▷ Randomly select adjacent times.

$\{(x_0, y_0), (x_1, y_1)\}_{b=1}^B \sim q(x_0, y_0|\tau_0), q(x_1, y_1|\tau_1)$

$\pi \leftarrow \text{OT}(\{(x_0, y_0), (x_1, y_1)\}_{b=1}^B)$ ▷ Interchangeable with Sinkhorn algorithm [38].

$\{(x_0^{(b)}, x_1^{(b)}), (y_0^{(b)}, y_1^{(b)})\}_{b=1}^B \sim \pi(z, w)$ ▷ Resample from time-specific OT coupling.

$t \sim \mathcal{U}(0, 1)$

$\tau \leftarrow \tau_0 + t(\tau_1 - \tau_0)$

$z = [(x_0^{(1)}, x_1^{(1)}), \dots, (x_0^{(B)}, x_1^{(B)})], \quad w = [(y_0^{(1)}, y_1^{(1)}), \dots, (y_0^{(B)}, y_1^{(B)})]$

$\alpha(w) \leftarrow \exp(-\|y_0 - y_1\|_2^2 / 2\sigma_y^2)$ ▷ Evaluate kernel for sampled conditioning values.

$p_t(x|z) \leftarrow \mathcal{N}(x; tx_1 + (1-t)x_0, \sigma_x^2 t(1-t))$

$p_t(y|w) \leftarrow \mathcal{N}(y; ty_1 + (1-t)y_0, \sigma_y^2 t(1-t))$

$x_t \sim p_t(x|z)$

$y_t \sim p_t(y|w)$

$u_t(x|z) \leftarrow ((1-2t)/(2t(1-t)))(x - (tx_1 + (1-t)x_0)) + (x_1 - x_0)$

$\nabla_x \log p_t(x|z) \leftarrow (tx_1 + (1-t)x_0 - x)/(\sigma_x^2 t(1-t))$

$\mathcal{L}_{\text{CVSFM}} \leftarrow \mathbb{E}_{t, q(z, w), p_t(x, y|z, w)} \left[\alpha(w) \left(\|v_\theta(x, y, \tau) - u_t(x|z)\|^2 + \lambda(t)^2 \|s_\theta(x, y, \tau) - \nabla_x \log p_t(x|z)\|^2 \right) \right]$

$\theta \leftarrow \text{Update}(\theta, \nabla_\theta \mathcal{L}_{\text{CVSFM}})$

end while

return v_θ, s_θ

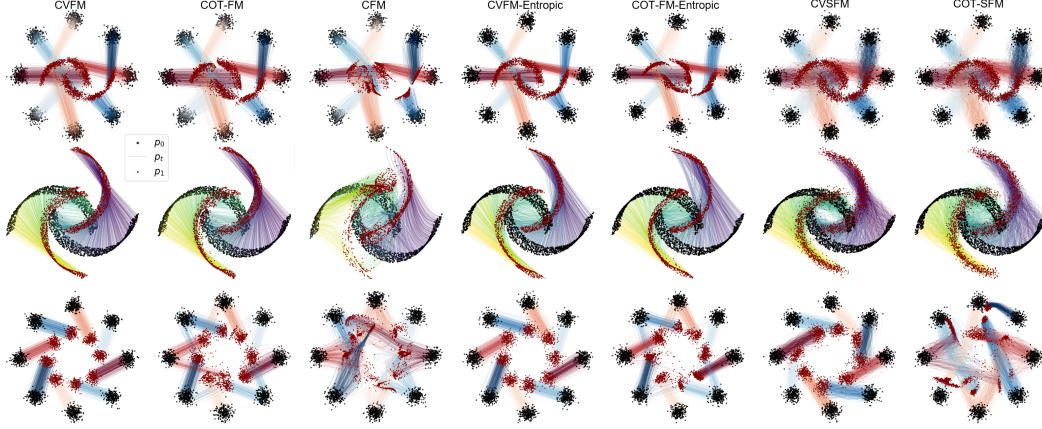


Figure E.1. Comparison of obtained trajectories for various OT and SB modeling approaches in the synthetic datasets considered associated with Wasserstein-2 error and normalized path energy reported in Table 1. Trajectories are colored by the conditioning variable. Source distributions are shown in black, target distributions are shown in maroon.

Mean absolute error values, along with minimum and maximum absolute error reported in Table 2 were evaluated on a test set of 2,000 microstructures, and a training set of 8,000 microstructures. Known state was compared against the expectation of the predicted conditional distribution over the state variable at a given time $\mathbb{E}[x_t|x_0, y]$.

All material specific cases used networks with five layers of width 256 and GELU activations [74]. Skip connections were applied over the middle three layers. The conditioning variable was subject to both self-attention and time cross-attention with an embedding dimensionality of 64 and 8 heads. The same network architecture was used in T-COT-FM, and for both drift and score networks in CVSFM, COT-SFM, and T-COT-SFM. It was duplicated for the NeuralODE benchmark. The LSTM benchmark consisted of four layers with width 512 for approximately equivalent parameterization. Optimization was carried out with cosine annealing of the learning rate from $1e-3$ to $1e-8$ and ADAM-W [75] with weight decay $1e-2$ and an effective batch size of 1024. Conditional probability paths were constructed with $\sigma_x = 0.1$, $\sigma_y = 0.1$, and mini-batch conditional OT was performed with $\eta = 100$. While, T-COT-FM in its initial formulation does not include a varying noise schedule across the conditioning variable, we have also included an ablation with this extension, mirroring the same value of σ_y .

E Appendix: Additional Case Study Specific Results

We move on towards presenting additional results obtained throughout this work. The results expand upon the discussion presented in Section 4 towards interrogating the empirical performance of CVFM, illuminating the critical advances necessary for learning conditional vector fields. We refer the reader to Appendix D for detailed descriptions of the datasets and training infrastructure used in each case study.

E.1 2D Experiments

In Figure 2 trajectories of the learned vector fields were presented for the *8 Gaussian - Moons* mapping with discrete conditioning and the *Moons - Moons* with continuous conditioning, although this remains a fraction of the cases run. For completeness, we present the trajectories of all methodologies evaluated in Table 1 in Figure E.1.

While, perhaps visually the simplest, the *8 Gaussian - 8 Gaussian* mapping, consisting of a 45 degree rotation about the origin, is demonstrably the most complex family of conditional vector fields to learn given samples of the empirical distribution $q(w, z)$. This is the only case in which only CVFM variants reliably learn to disentangle the conditional dynamics (Figure E.1), while COT-FM attempts

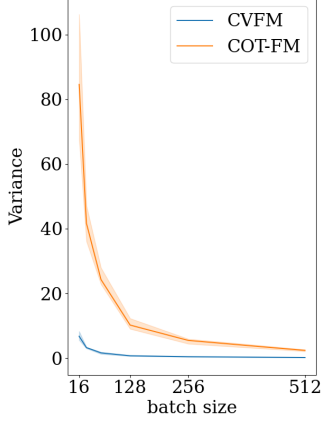


Figure E.2. Objective variance across batch sizes in the *8 Gaussian-8 Gaussian* case.

Table E.1. Variance of the conditional objective across the synthetic datasets considered swept across varying batch sizes. Variance values were computed over 5 seeds with a conditioning transport weight of $\eta = 10$. Values are reported as $\mu \pm \sigma$.

	Batch Size	8 Gaussian-8 Gaussian	8 Gaussian-Moons	Moons-Moons
CVFM	16	6.465 \pm 0.561	7.847 \pm 1.405	0.699 \pm 0.157
	32	2.896 \pm 0.364	3.618 \pm 0.142	0.179 \pm 0.030
	64	1.515 \pm 0.200	1.648 \pm 0.268	0.044 \pm 0.007
	128	0.678 \pm 0.0517	0.946 \pm 0.099	0.014 \pm 0.002
	256	0.379 \pm 0.086	0.493 \pm 0.057	0.005 \pm 0.0005
	512	0.175 \pm 0.032	0.216 \pm 0.043	0.002 \pm 0.0004
COT-FM	16	77.376 \pm 12.805	17.780 \pm 2.657	3.243 \pm 0.356
	32	42.891 \pm 4.948	7.482 \pm 0.857	1.561 \pm 0.154
	64	21.197 \pm 0.802	4.468 \pm 0.621	0.739 \pm 0.043
	128	9.672 \pm 2.178	1.791 \pm 0.266	0.369 \pm 0.049
	256	5.383 \pm 0.588	1.057 \pm 0.037	0.191 \pm 0.026
	512	2.718 \pm 0.475	0.563 \pm 0.045	0.094 \pm 0.012

to split mass to minimize transport costs across the joint $\mathcal{X} \times \mathcal{Y} : \mathbb{R}^N \times \mathbb{R}^M$, visualized by splits mapping to target densities with similar conditioning values.

Objective Target Variance: One reason for the improved convergence of CVFM is the significantly lower variance of the training objective target in CVFM in comparison to COT-FM. We define the objective target variance (OTV) as

$$\begin{aligned} \text{OTV}_{\text{CVFM}} &= \mathbb{E}_{t,q(z,w),p_t(w),p_t(x,y|z,w)} \|u_t(x|z)\|^2 \\ \text{OTV}_{\text{COT-FM}} &= \mathbb{E}_{t,q(z,w),p_t(x,y|z,w)} \|u_t(x|z)\|^2 \end{aligned} \quad (\text{E.1})$$

Notably, these equations do not include the true underlying conditional vector field and, as such, the computed values should not be compared across test cases. Figure E.2 demonstrates the stark contrast between COT-FM and CVFM on the *8 Gaussian - 8 Gaussian* case, while Table E.1 details results for all 2D synthetic cases. This significant reduction in the target conditional vector field variance enables the objective to provide consistent gradients during training of the network, enabling improved convergence towards identifying the correct disentangled latent dynamics.

Conditioning Mismatch Kernel: The conditioning mismatch kernel $\alpha(w)$ plays a pivotal role in the objective introduced in Eq. (10), which we duplicate here in its complete form.

$$\mathcal{L}_{\text{CVFM}}(\theta) = \mathbb{E}_{t,q(z,w),p_t(x|z)p_t(y|w)} [\alpha(w) \|v_\theta(x, y, t) - u_t(x|z)\|^2] \quad (\text{E.2})$$

The selected form of this kernel dictates the degree of continuity expected *a priori* in the observed joint vector fields $u_t(x, y)$ across $y \in \mathbb{R}^M$, introducing an inductive bias in the solution across this joint space, even if we only ever expect to evaluate the vector field in a conditional sense. In this work, we select $\alpha(w) = \exp(-\|w\|_2^2 / 2\sigma_y^2)$ with observation $w = y_1 - y_0$, where the degree of continuity in u_t across the conditioning variable can be tailored through an appropriate selection of σ_y .

Previously, in Table 1, we observed significantly improved performance with the introduction of this additional rebalancing – which naturally raises questions as to its contribution in isolation. Figure E.3 demonstrating that even by itself in the absence of mini-batch OT, the introduction of $\alpha(w)$ is able to reliably equal or improve upon Wasserstein-2 target distribution error in comparison with COT-FM and CVFM. Figure E.4 similarly shows an evaluation across η values (the weighting in the optimal transport ground cost), highlighting the stability it introduces across all test cases relative to mini-batch OT solves with Eq. (12). In the *8 Gaussian - 8 Gaussian* case, $\alpha(w)$ drastically outperforms COT-FM, with comparable performance in the other mappings, albeit without providing approximate OT within the conditioned vector fields. Due to this limitation, one might view $\alpha(w)$ in isolation as a reliable extension to conditional CFM.

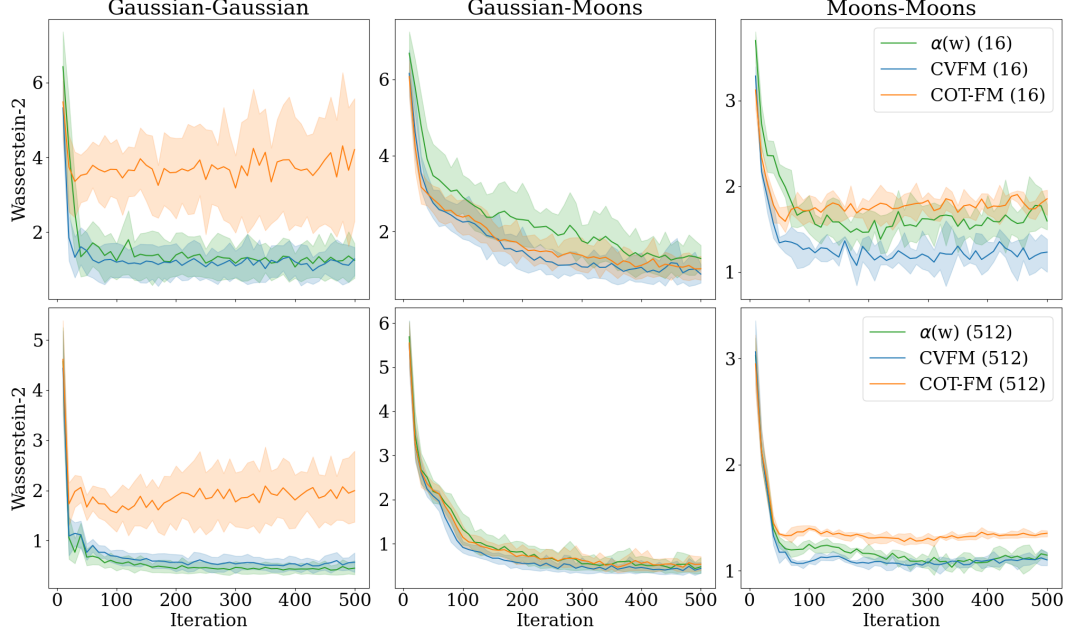


Figure E.3. Demonstration of the effectiveness of performing an expectation of the objective with solely $\alpha(w)$ in comparison to the COT-FM and CVFM approaches. The use of $\alpha(w)$ in isolation is better able to disentangle associated conditioning variables in almost all cases than the conditional Wasserstein distance introduced in Eq. (12).

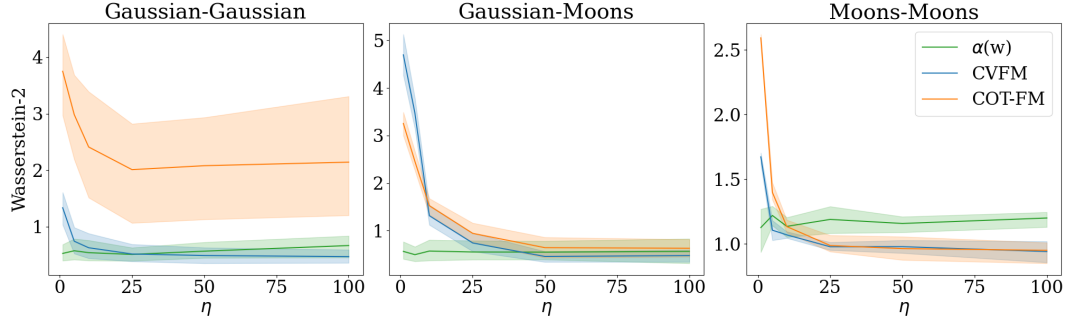


Figure E.4. $\alpha(w)$ more reliably reduces Wasserstein-2 error to the target distribution in comparison with COT-FM across values of η .

E.2 MNIST-FashionMNIST Domain Transfer

In this section, we further interrogate the results presented in Figures 2 and E.2, and their implications in higher dimensional distributional mappings. The results previously presented in Figure 3 illustrated the convergence characteristics of CVFM and COT-FM measured using conditional image metrics. The improved convergence with increasing η of COT-FM only further reinforces the value of ground cost scaling across η . Unfortunately, the optimal value of η is problem dependent, and is particularly challenging to identify a priori. The conditional scaling kernel ameliorates these difficulties. As shown in Figure E.2, the kernel significantly reduces the objective variance in comparison with conditional OT, facilitating stable convergence upon more accurate conditional OT mappings. This behavior was first observed in 2D examples in Figures 2 and E.1 and such characteristics extend to the high-dimensional setting. This increased stability facilitates a greater tolerance on η values, ameliorating potential difficulties during hyperparameter optimization. In Figure E.5, we observe this stability through the inspection of randomly generated samples from mapping the first class of MNIST to the first class of FashionMNIST. While in an unconditional sense, COT-SFM with $\eta = 10$ is able to appropriately transfer between MNIST and

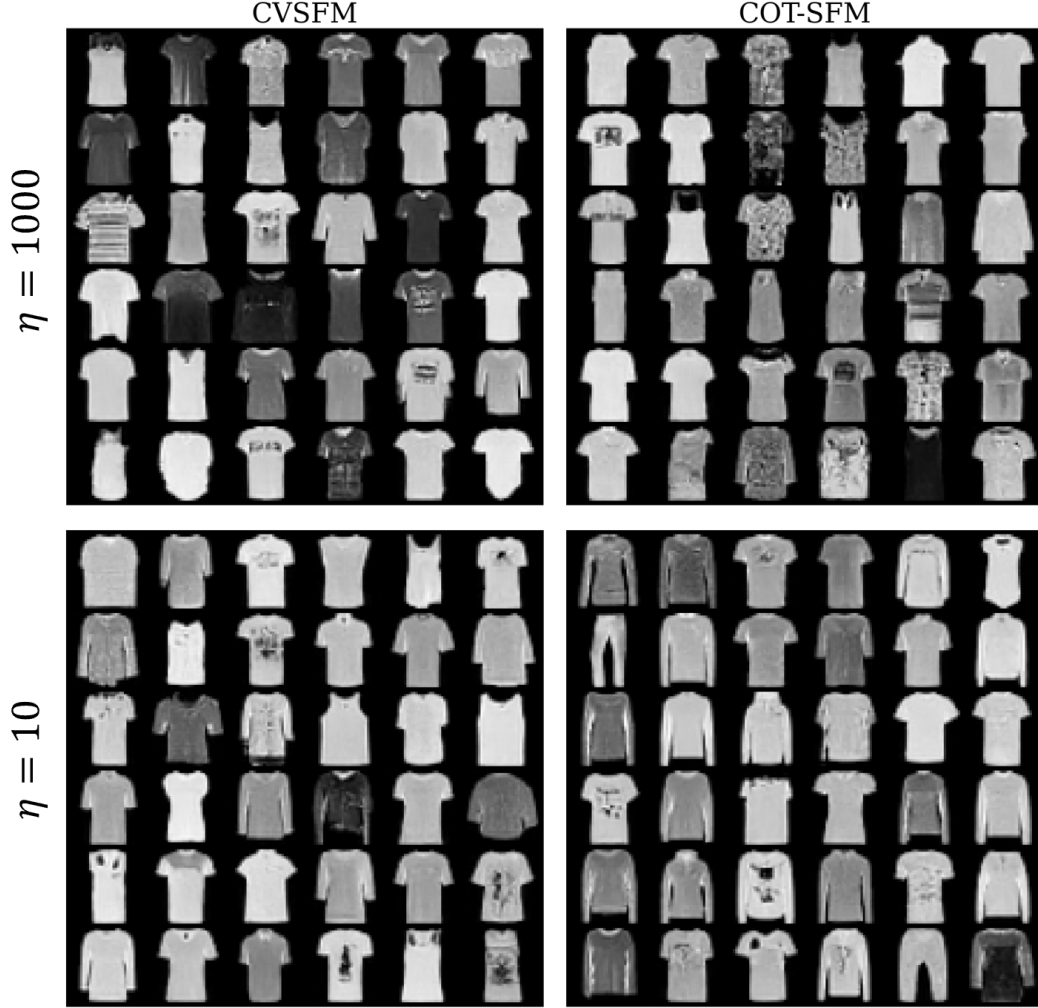


Figure E.5. Comparison of 32 randomly generated images corresponding to the first class of FashionMNIST with CVSFM and COT-SFM for $\eta = 10$ and $\eta = 1000$.

FashionMNIST, its consistency in mapping to the correct conditional distribution is lost without elevated penalization in transport across y . In comparison, CVSFM is able to consistently map to t-shirts/tops in the first class even with orders of magnitude difference in η . Similarly, in Figure 3, the convergence behavior for CVFM degrades very little with large changes in η .

Figure 3 displayed the convergence characteristics of conditional FID and LPIPS scores, conditionally evaluated for each class of $p_1(x|y)$, only serving to reinforce the prior discussion. In comparison, in evaluating FID scores for $p_1(x) = \int p_1(x|y)p(y)dy$, distinctions in the performance between CVSFM and COT-SFM are removed. Figure E.6 highlights the equivalence in unconditional performance in this case study across 10,000 images. This discrepancy in conditional to unconditional FID scores highlights limitations of mini-batch sampling from the conditional OT coupling $\pi_\eta((x_0, y_0), (x_1, y_1))$. Even with elevated weighting on transport in the conditioning variable, mini-batch conditional OT provides a poorer approximation.

Table E.2. Comparison of conditional mean (FID) and unconditional FID scores (FID-All) for 10,000 samples alongside conditional LPIPS scores.

Model	FID-All (\downarrow)	FID (\downarrow)	LPIPS (\downarrow)
CVSFM ($\eta = 1000$)	11.668	32.915	0.159
COT-SFM ($\eta = 1000$)	14.965	36.456	0.161
CVSFM ($\eta = 10$)	23.554	48.326	0.175
COT-SFM ($\eta = 10$)	15.751	94.690	0.232

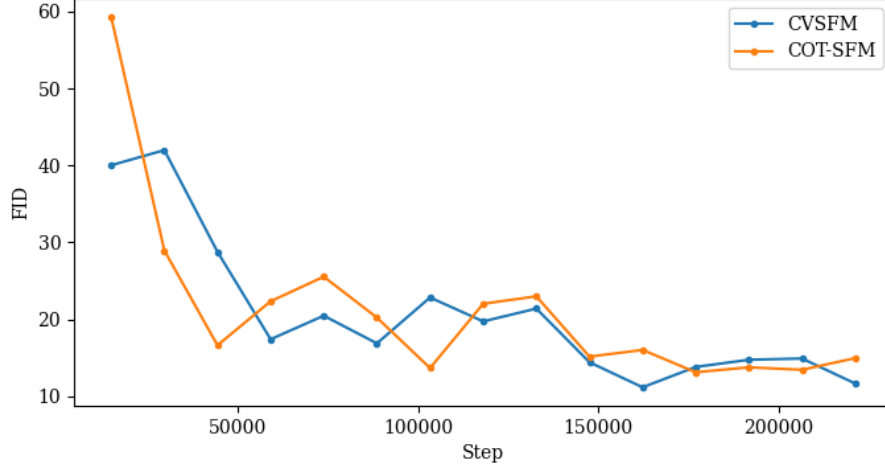


Figure E.6. Unconditional FID scores evaluated across 10,000 samples $x \sim p_1(x)$ for COT-SFM and CVSFM ($\eta = 1000$) during training.

E.3 Material Dynamics

The mean absolute error metrics displayed in Table 2 provide point estimates of the performance of our proposed method, providing evidence that we are capable of reliably disentangling the latent processing dynamics of material microstructures across the conditional processing space, given unpaired samples of process conditions and material state observed at discrete times. For further interrogation, we present the estimated error distributions in Figure E.7 across all 2,000 material samples in the test set. In congruence with the results presented earlier, CVSFM-exact outperforms all other methods, a surprising fact given the stochastic nature of only viewing observations sampled from $q(z, w, \tau)$. The Neural ODE [36] outperforms other methods, approximately matching the performance of the most optimal CVSFM-Exact variant (i.e., exhibiting similar tails and a mean shift). Figure E.8 compares the dynamics predicted by the three models on several selected members of the test dataset. Mirroring the distribution of errors in Figure E.7, the CVSFM model slightly outperforms the other two while also providing uncertainty estimates. The panels in Figure E.8 display the dynamics projected onto individual principal component subspaces, α_i .

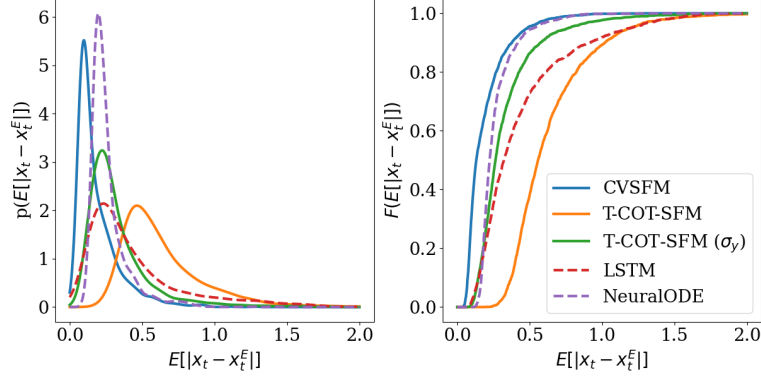


Figure E.7. (Left) probability density function, and (right) cumulative distribution function of CVFSM in comparison with evaluated conventional approaches requiring complete trajectory information.

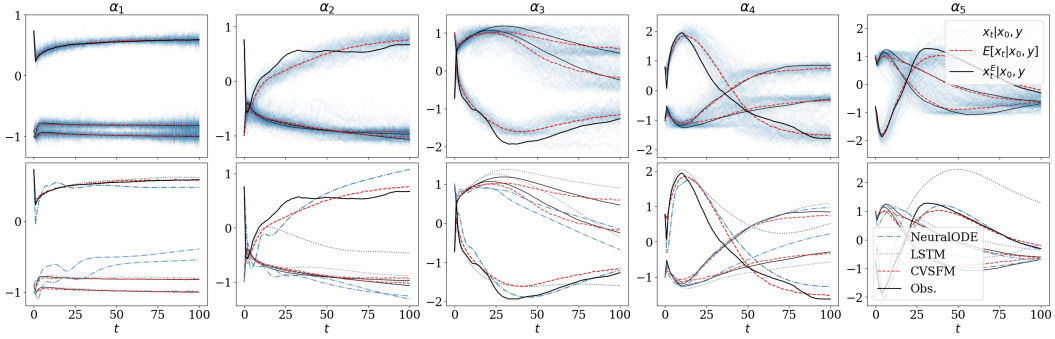


Figure E.8. Collection of three randomly sampled trajectories from the test set in PC space displaying (top) 128 samples in blue from CVFSM, with the expected value in red, and (bottom) deterministic predictions of the LSTM and Neural ODE shown against the expected value of CVFSM.